Synthesis and characterization of $Cu_{1-x}Ni_xO/Fe_2O_3$ composite from plant-mediated Ni-doped CuO and Fe_2O_3 for degradation of Methylene blue

Ermias Tafa Debele

A Thesis Submitted to

The Department of Materials Science and Engineering
School of Mechanical, Chemical, and Materials Engineering

Presented in Partial Fulfillment of the Requirement for the Degree of

Master's in Materials Science and Engineering

Office of Graduate Studies
Adama Science and Technology University

Adama, Ethiopia
May 2022 G.C

Synthesis and characterization of $Cu_{1-x}Ni_xO/Fe_2O_3$ composite from plant-mediated Ni-doped CuO and Fe_2O_3 for degradation of Methylene blue

Ermias Tafa

Advisor

Dr. Temesgen Debelo

Co-Advisor

Dr. Osman Ahmed

A Thesis Submitted to

The Department of Materials Science and Engineering
School of Mechanical, Chemical, and Materials Engineering

Presented in Partial Fulfillment of the Requirement for the Degree of

Master's in Materials Science and Engineering

Office of Postgraduate Studies

Adama Science and Technology University

Adama, Ethiopia
May 2022 GC

DECLARATION

I hereby declare that this Master Thesis entitled ***"Synthesis and characterization of $Cu_{1-x}Ni_xO/Fe_2O_3$ composite from plant-mediated Ni-doped CuO and Fe_2O_3 for degradation of Methylene blue"*** is my original work. That has not been submitted for the award of any academic degree, diploma, or certificate in any other university. All sources of materials that are used for this thesis have been duly acknowledged through citation

Name of student	Signature	Date

RECOMMENDATION

We, the advisors of this thesis, hereby certify that I have read the revised version of the thesis entitled ***"Synthesis and characterization of $Cu_{1-x}Ni_xO/Fe_2O_3$ composite from plant-mediated Ni-doped CuO and Fe_2O_3 for degradation of Methylene blue"*** prepared under my guidance by Ermias Tafa Debele submitted in partial fulfillment of the requirements for the degree of Masters of Science in **Materials science and engineering**. Therefore, I recommend the submission of a revised version of the thesis to the department following the applicable procedures.

_____	_____	_____
Major Advisor	Signature	Date
_____	_____	_____
Co-advisor	Signature	Date

APPROVAL SHEET

I/We, the advisors of the thesis entitled "***Synthesis and characterization of $Cu_{1-x}Ni_xO/Fe_2O_3$ composite from plant-mediated Ni-doped CuO and Fe_2O_3 for degradation of Methylene blue"*** and developed by **Ermias Tafa Debele** ID No: PGR/21825/13, here by certifying that the recommendation and suggestions made by the board of examiners are appropriately incorporated into the final version of the thesis.

Major Advisor	Signature	Date
Co-Advisor	Signature	Date

We, the advisors of the thesis entitled ***"Synthesis and characterization of $Cu_{1-x}Ni_xO/Fe_2O_3$ composite from plant-mediated Ni-doped CuO and Fe_2O_3 for degradation of Methylene blue"*** and developed by **Ermias Tafa Debele** hereby certify that the recommendation and suggestions made by the board of examiners are appropriately incorporated into the final version of the thesis.

Chairperson	Signature	Date
Internal examiner	Signature	Date
External examiner	Signature	Date

Finally, approval and acceptance of the thesis are contingent upon the submission of its final copy to the Office of Postgraduate Studies (OPGS) through the Department Graduate Council (DGC) and School Graduate Committee (SGC).

Department Head	Signature	Date
School Dean	Signature	Date
Office of Postgraduate Studies	Dean Signature	Date

ACKNOWLEDGMENTS

First and foremost, I could not have undertaken this journey without my advisor Dr. Temesgen Debelo. He always makes time to answer questions and give highly helpful criticism, regardless of his schedule. Words cannot express my gratitude to my co-advisor Dr. Osman Ahmed Zelekew, for his patience, guidance, friendly attitude, and sharing of good ideas.

I would like to express special thanks to and appreciation to Dr. Gebisa Bekele, the head of the Materials Science and Engineering (MSE) department, for his advice and for discussing correcting the path that I were, his constructive criticism, valuable suggestions, and overall guidance have a high weight throughout the whole studies.

And my special thanks go to Mr. Hayleyesus Hatano for providing Acmella Ciliate plant, giving sizable answer and special support by losing his time. I am also grateful to Mr. Demeke Tesfaye, for his inspiring support and facilitation throughout all of lab activities during my thesis work. I am feeling grateful to all staff members of the MSE Department; especially, Dr. Dinsefa Mensur Andoshe, Mr. Henok Girma, and Mr. Kamil Esleman, for their kindly encouragement, and true friendship support throughout this research work.

I found no words to express my deepest gratitude to my family, especially my brother Mr. Amare Tafa and all family members for their never-ending love, effort, blessing, and support financially they have a lion's share in my achievements. Last but not least, I would like to acknowledge all of my friends: especially Mr. Mintesinot Tamiru, and all my classmates for their kindly encouragement, motivation, and sharing their helpful thoughts for the achievement of my thesis work.

TABLE OF CONTENTS

LIST OF FIGURES

LIST OF TABLES

LIST OF ACRONYMS

AOPs	Advanced Oxidation Process
BET	Bruneur Emmit Teller
CB	Conduction Band
CuO	Copper Oxide
DTA	Differential Thermal Analysis
E_g	Energy Band gap
EIS	Electrochemical Impedance Spectroscopy
Fe_2O_3	Iron Nitrate
FWHM	Full Width at Half Maximum
FTIR	FTIR - Fourier Transformation Infrared Spectroscopy
h	hour
MB	Methylene blue
NHE	Normal Hydrogen Energy
$O_2^{\bullet}$	Oxygen Radical
$OH^{\bullet}$	Hydroxyl radical
PL	Photo Luminescence
SEM	Scanning Electron Microscope
TEM	Transmission Electron Microscope
TGA	Thermo Gravimetric Analysis
UV-VIS	Uv Visible Spectroscopy
VB	Valence band
XRD	X-ray Powder Diffraction
^oC	Degree Centigrade
V	Frequency
θ	Half diffraction angle

ABSTRACT

Water pollution is a widespread serious environmental issue that we face on a global scale. The increased demand for clean water amplified the importance of removing toxic organic pollutants from wastewater sources. These toxic chemicals can be transformed into non-toxic substances by degradation using a photocatalytic process. For this, different oxide materials have been used. Among these materials, Copper oxide (CuO) is one of the most widely used oxide for the degradation of methylene blue (MB) organic dye molecules from wastewater. However, there are challenges with the usage of CuO for photo-catalysis such as charge carrier's recombination which resulted in lowering the degradation efficiency. To overcome this problem, Acmella Ciliate plant-mediated Ni-doped CuO was synthesized and a composite was formulated, i.e., $Cu_{1-x}Ni_xO/Fe_2O_3$ (x = 0.01, 0.02, 0.03, 0.04). The samples were subjected to characterizations such as X-ray Diffraction (XRD), Thermo-gravimetric analysis (TGA), and Fourier-Transform Infrared (FTIR). Scanning Electron Microscopy (SEM), Brunauer Emmett-Teller (BET), Photoluminescence (PL), Electrochemical Impedance Spectroscopy (EIS), and UV- Vis spectroscopy have been used. The optical bandgap of the synthesized CuO, 2NCO, Fe_2O_3, and (60%) 2NCO/40%Fe_2O_3 was found to be 2.2, 2.17, 2.3, and 1.7 eV, respectively. The absorbance and degradation performance of Ni-doped CuO against MB was analyzed and the 2% Ni-doped CuO yielded an optimum result. Therefore, the 2% Ni-doped CuO (2NCO) was further used for the establishment of a composite with Fe_2O_3. The nominal composition of the oxide composite was (1-x) 2NCO/(x) Fe_2O_3 (x=0.1, 0.2, 0.3, 0.4, and 0.5). The degradation performance of these oxide composites was determined against MB and the sample with the nominal composition of (60%) 2NCO/40%Fe_2O_3 resulted in an optimum degradation percentage of 94%. The recyclability test was performed for 5 cycles using the (60%) 2NCO/40%Fe_2O_3 and the sample remained stable. Therefore, according to the present finding, the plant-mediated Ni-doped CuO and Fe_2O_3 materials systems can degrade MB organic dye from industrial effluents.

Key words: Photocatalyst, Water pollution, Acmella Ciliate, Methylene Blue, and dye degradation

CHAPTER ONE
1. Introduction

1.1 Backgrounds of the study

Many major environmental concerns that we face on a worldwide scale have been the subject of considerable concern in recent years. One among them is the protection of our most valuable natural resource water. The need of eliminating organic contaminants and harmful heavy metal ions from water sources has increased in response to the rising demand for clean water[1]. Organic dyes are azo dyes commonly used in the textile, food, paper, leather, printing, and pharmaceutical industries. Methylene blue is organic contaminants has devastating environmental effects due to its toxicity, carcinogenicity, mutagenicity, non-biodegradability, and complex chemical structure. As a result, before being discharged into the environment, these contaminants must be removed and/or converted to non-toxic molecules as efficiently as possible[2].

Several techniques for removing and converting these contaminants have been developed. Some of these processes are flocculation, adsorption, biodegradation, sedimentation, membrane process, and so on[3]. Adsorption is a surface process that causes a molecule to move from a fluid bulk to a solid surface physical forces or chemical bonds can cause this to happen. When it is reversible (the opposite process is called desorption), it is responsible not only for substance subtraction but also for substance release[4]. Biodegradation is a natural process that recycles biologically important components on a continuous basis. Microbes in the Earth's crust play a major role in these biogeochemical cycles. Enzymes that are organized in pathways that transform compounds via a sequence of intermediates into end products commonly catalyze biodegradation processes. Mineralization is the process of converting a chemical into fully oxidized compounds[5]. Membrane processes are advanced filtration methods that take advantage of the separation properties of finely porous polymeric or inorganic films. Membrane separations are used to separate biological macromolecules, colloids, ions, solvents, and gases in a variety of industrial processes. However, due to the complex composition and different physicochemical properties of the contaminant. Those techniques are insufficient due to low efficiency, high energy consumption, and risk of secondary pollutant formation[6]. Furthermore, due to the presence of stable aromatic groups in the structure of organic pollutants, they are non-degradable using traditional techniques[7]. As a result, an alternative technique that is high in efficiency, low in

energy consumption, and environmentally friendly for the treatment of industrial effluents to remove and convert them to non-toxic molecules and substances is desirable. Photocatalysis, which uses photon energy and oxide semiconductor nanomaterials as a catalyst to degrade organic contaminants, is one of the alternative approaches to treating industrial contaminants[8].

Metal oxides such as TiO_2, ZnO, CeO_2, CuO, Fe_3O_4, Fe_2O_3, $BiVO_4$, and others have been studied for their photocatalytic activity due to the degradation of various organic pollutants[9-12]. Catalysis by metal oxides under solar irradiation is primarily limited by a large bandgap, low charge transfer efficiency, poor photo corrosion resistance, and low recyclability. Heterojunctions are created through composite synthesis, metal/nonmetal doping, and so on. Green technology based on plants is becoming more popular as an eco-friendly, non-toxic, cost-effective, and safe option, because plant extract-mediated biosynthesis of nanoparticles provides natural capping agents in the form of protein[13]. CuO and α-Fe_2O_3, two important transition metal oxides, have been extensively studied and applied in a variety of fields, including catalysts[14], sensors[15], and electrochemistry[16]. Many methods have been used to create CuO/Fe_2O_3 composites, including solid-phase reaction[17], hydrothermal[18], co-precipitation[19], sol-gel method[20]. The green synthesis method has advantages over other synthesis techniques due to its high yield, high product purity, no need for organic solvents, easy reproducibility, low cost, and environmentally friendly approach[21].

Recent research indicates that the photon property of CuO plays an important role due to the variable oxidation states of copper, i.e., Cu^{+}, Cu^{2+}, and Cu^{3+}, which allows for both hole and electron doping[22]. Many changes have been reported as a result of transition metal doping into the CuO lattice, such as Ni-doping, Fe-doping, Ti-doping, Cd-doping, and Zn-doping[23]. Transition metal ions can generate energy states within the bandgap. To overcome the limitation of metal oxide for photocatalytic application. Ni-doped CuO is an interesting material for improving visible light absorption. Furthermore, these serve as intermediate steps for electrons as they move between the valence and conduction bands[22, 24].

In this work, Synthesis and characterization of $Cu_{1-x}Ni_xO/Fe_2O_3$ composites from and plant-mediated Ni-doped CuO and Fe_2O_3 for degradation of Methylene blue. The Plant type *Acimalla Ciliate* was used as a capping/stabilizing agent.

1.2 Statement of the problem

Nowadays, the need for efficient and recoverable photo catalysts for organic dye removal from industrial wastewater is a challenging problem. $Cu_{1-x}Ni_xO/Fe_2O_3$ is a promising material in visible light absorption. However, the photocatalytic performance of CuO is limited by the rapid charge recombination because of its lower bandgap energy (1.9 eV/NHE). To inhibit the charge carrier recombination of CuO, many research works have been done. Among them, 2NCO coupled with Fe_2O_3 effectively enhances the photocatalytic performance of CuO due to a longer recombination time. Green synthesis of CuO and Fe_2O_3 employing the Acmella Ciliate plant as a capping/stabilizing agent to boost the catalyst's specific surface area. Furthermore, doping and coupling with Fe_2O_3 improve charge transfer capabilities in the $Cu_{1-x}Ni_xO/Fe_2O_3$ process.

1.3 Objectives

1.3.1 General objective

Synthesis and characterization of $Cu_{1-x}Ni_xO/Fe_2O_3$ composite from plant-mediated Ni-doped CuO and Fe_2O_3 for degradation of Methylene blue.

1.3.2 Specific objectives

- ✓ Extraction of *Acmella Ciliate* plant leaf and synthesis of CuO using the extract solution.
- ✓ Synthesis of plant-mediated Ni-doped CuO with different dopant percentages (1, 2, 3, and 4%) and Fe_2O_3 using green synthesis methods.
- ✓ Synthesis of composite $(1-x)2NCO/(x)Fe_2O_3$ with a different weight percentage of *(*x=0.1, 0.2, 0.3, 0.4, and 0.5).
- ✓ Characterizations of the synthesized samples with XRD, TGA-DTA, FTIR, SEM, BET PL, EIS, and UV-VIS.
- ✓ Evaluate the photocatalytic degradation efficiency of the synthesized photocatalytic materials against the methylene blue (MB).

1.4 The scope of the research

The extraction of the Acmella Ciliate plant and synthesis of CuO and Fe_2O_3 employing plant extract as a stabilizing/capping agent was carried out in this study. Ni-doped CuO was made with different doping concentrations. The optimized Ni-doped CuO was composed of different

concentrations of Fe_2O_3 using a simple biosynthesis method. Finally, the performance evaluation of the synthesized samples was investigated using MB dye.

1.5 Significance of the study

This work primarily helps sectors that produce an effluent with high concentrations of MB organic dye such as textile, paper, cosmetics, and leather manufacturing. Additionally, the pollution caused by this MB will be decreased. The deterioration of a discharged organic pollutant reduces human exposure to the contaminant and reduces the amount of oxygen that the contaminant can absorb. Organic dye MB-related problems such as cancer, mutation, and skin irritation could be reduced from a human health standpoint.

CHAPTER TWO

2. Literature Review

2.1 Wastewater

Environmental pollution caused by industrial wastewater is now a major concern and priority for the entire world, particularly in industrialized nations. Industrial wastes, mining activities, pesticides, and chemical, fertilizers, contribute significantly to water pollution and environmental pollution in general[25]. As a result of the processes that use various types of chemicals and the exposure of the water to microorganisms. Radioactive, chemical, and microbial contaminants are the three types of water pollutants. The ingestion of these contaminants hurts human health pathogenic contaminants frequently cause gastro interstitial illness. while chemical contaminants can damage major organs, and functional systems, and increase the risk of cancer. Among these are chemical contaminants, which have a credible effect on human health and are released in trace amounts by industries[26]. The organic contaminant is a type of chemical contaminant that is hazardous to humans due to the contaminant's difficult degradability due to the aromatic groups in the structure of the organic pollutants[27]. Figure 1 depicts the classification of the various types of contaminants that pollute water. Organic dyes are one of the organic contaminants released by various industries. These contaminants have the potential to cause mutation, cancer, and skin irritation. They also reduce the amount of oxygen in the water, which causes an ecological problem. As a result, industrial wastewater must be effectively treated for the sake of human and environmental well-being[28].

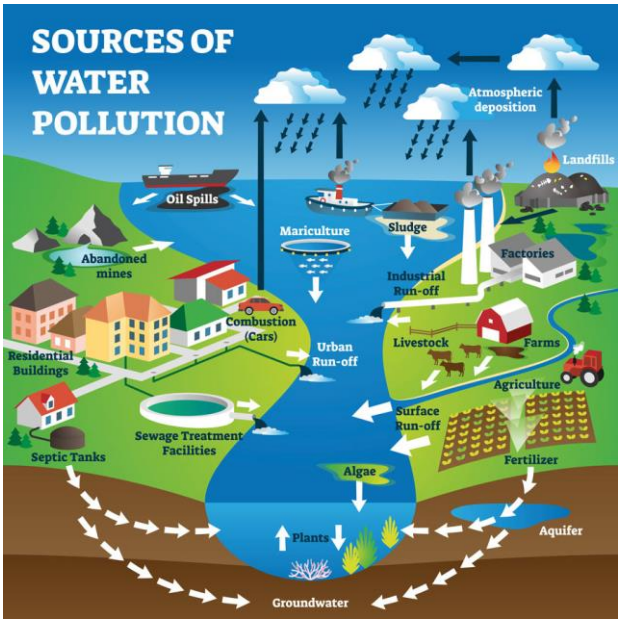

Figure 1. *Types of water contaminants[29].*

2.2 Photocatalysis

A photocatalytic reaction is accelerated by light energy in the presence of semiconductor material. As shown in Figure 2 The induced light generates electrons and holes from the semiconductor, which are then used to produce hydroxide radicals, which degrade the pollutant into carbon dioxide and water[30]. Because of the following factors, the evolution of a new branch of science known as nanoscience has completely replaced previous technologies. Most organics are completely mineralized by nanomaterials, which are also inexpensive. Semiconductors completely remove organic matter from polluted water. Nano photocatalysts are non-toxic, non-corrosive, and chemical and thermally stable [31]. Photocatalysts are widely available, cheap, and resistant to corrosion in the presence of water and chemicals[32].

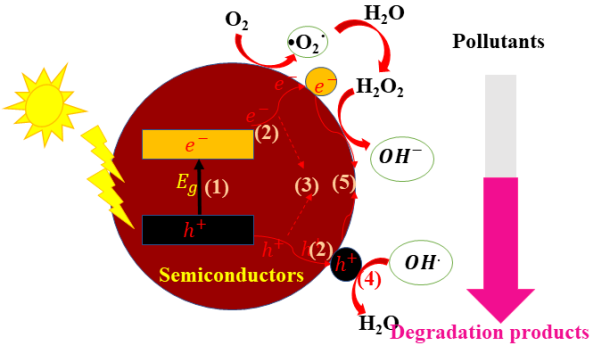

Figure 2. *Schematics representation of the electronic structure of semiconductors.*

2.3 Wastewater treatment techniques

2.3.1 Conventional wastewater treatment technology and their drawbacks

The traditional treatment methods for these effluents are split into three categories: biological, chemical, and physical. These traditional effluent treatment procedures are inefficient because they either do not remove all of the colors or are ineffective on contaminants that are not readily adsorbable or volatile. Furthermore, they have additional disadvantages because they merely shift contaminants to another phase, causing disposal issues. Biological treatment necessitates a huge amount of land and is limited by diurnal sensitivity as well as the toxicity of some chemicals, as well as a lack of design and operating flexibility[33]. Chemical methods consume a lot of chemicals and produce a lot of sludge, which needs to be treated as well this procedure is also quite costly. Membrane filtration operations (nanofiltration, reverse osmosis, electrodialysis, etc.) and adsorption techniques are common. The fundamental disadvantage of membrane processes is that they have a finite lifespan before membrane fouling occurs, necessitating periodic replacement, which must be factored into any economic viability study. Liquid-phase adsorption is one of the most extensively utilized methods for removing pollutants from wastewater. Activated carbon is extensively employed as an adsorbent in the treatment of water and wastewater. Activated carbon adsorption, on the other hand, has a high ongoing expense. The difficulty of extracting this material from wastewater after use is one of the two main disadvantages of using it[34].

2.3.2 Advanced oxidation process

Advanced oxidation processes (AOPs) are widely used to remove organic constituents that are difficult to remove from industrial and municipal wastewater. AOP-type procedures, in this sense, have the potential to be very promising technologies for treating wastewater containing non-biodegradable or barely biodegradable organic compounds with high toxicity[35]. These methods rely on the production of highly oxidative OH radicals in the reaction medium. The preferential use of H_2O_2 as an oxidative agent and OH radical generator. This is justified by the ease with which hydrogen peroxide can be stored, transported, and used, as well as the procedure's safety and efficiency[6].

Filtration is another type of effluent treatment method that uses clay, membranes, or nanomaterials to separate contaminants from waste water. However, due to the composition of

organic contaminants, filtration is ineffective in its removal. Organic dye degradation can be accomplished through the use of ozonation and the Fenton reaction. However, the Ozonation process requires a lot of electricity, which is expensive, and the Fenton method produced secondary pollution like iron sludge[36]. The hydroxyl radical (OH•) is a potent, non-selective chemical oxidant that reacts quickly with almost all organic molecules. With an oxidation potential of 2.8 V vs NHE, the hydroxyl radical is the second strongest known oxidant after fluorine (Normal Hydrogen Electrode). It can oxidize and mineralize practically any organic molecule, releasing CO_2 and inorganic ions in the process[37].

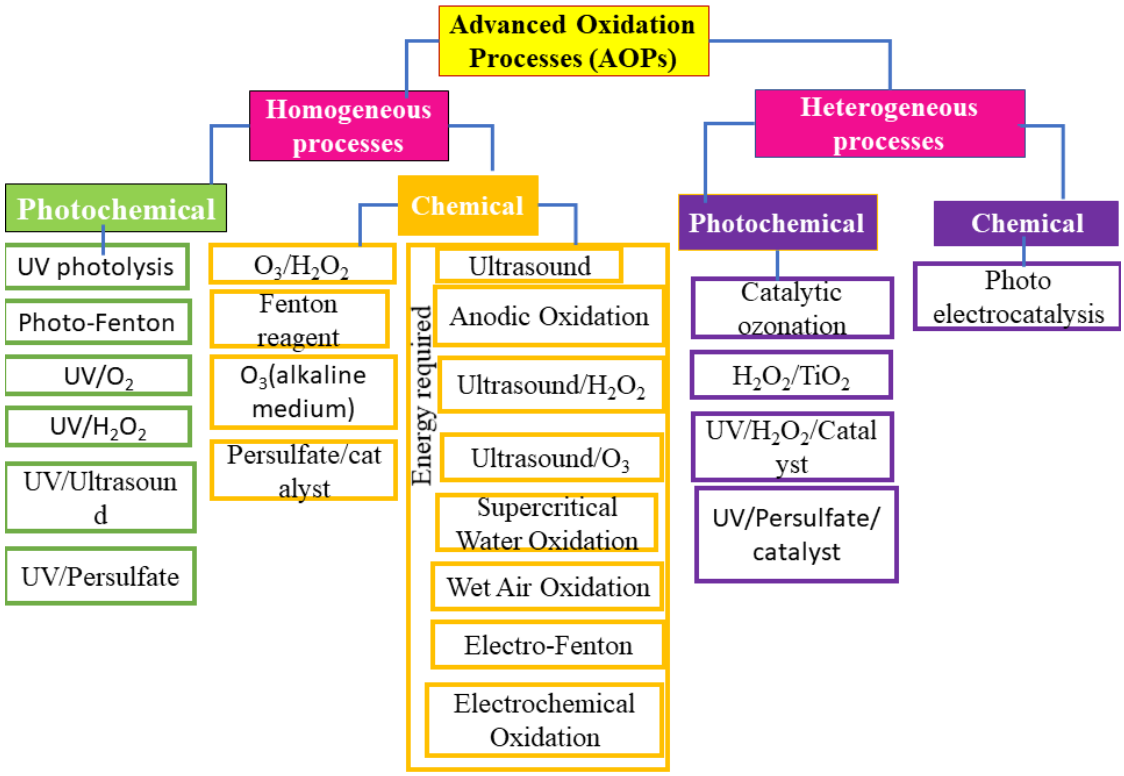

Figure 3. *Classification of Advanced Oxidation Process.*

2.4 Electronic structure of semiconductor photocatalysts

The quantum numbers *n*(shells), *l* (subshells), m_l (number of states in each subshell), and m_s (spin moment, +1/2, and -1/2) characterize discrete electronic energy states in an isolated atom. When two atoms are nearby, the electrons surrounding each atom begin to interfere with each other, beginning with the outer shell electrons. Pauli Exclusion Principle, states that each quantum state in an electron system such as an atom, molecule, or crystal can be occupied by no more than one electron, and each energy level will split into two. Instead of two atoms, a

solid is an assembly of a large number N of atoms. As a result, when N atoms are brought close together, the identical energy levels in isolation split into N closely spaced but distinct energy levels[38]. Because the maximum and minimum energy allowed for each orbital is determined by nearest-neighbor interactions. Rather than the number of atoms, the energy "width" over which these levels can split is limited. When N is large, the levels are so close together that they can be thought of as a continuum of energetic states forming an "electronic energy band". Figure 4 depicts how the electronic structure of a semiconductor compound changes as the number N of monomeric unit's present increases from one to a cluster of more than 2000 units. As a result, the electronic energy structure within a semiconductor is divided into three distinct regimes: the conduction band (CB), the valence band (VB), and the forbidden band. The forbidden band denotes a region in which no energy states exist for an ideal, undoped semiconductor. There are only two energy states: above and below this region. The higher band is referred to as the conduction band, while the lower band is referred to as the valence band, using the energy level of an electron in a vacuum as a reference and as the topmost level[39].

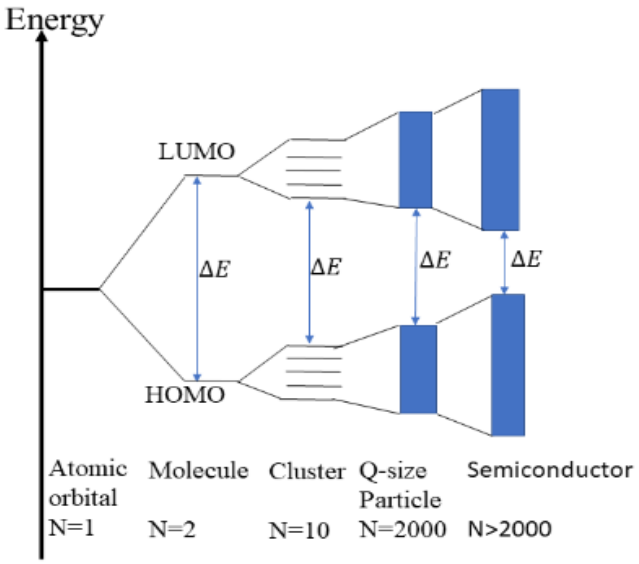

Figure 4. *Change of the electronic structure of a semiconductor compound as the number N of monomeric unit's present increases from unity to clusters of more than 2000 units.*

Thermal or optical excitation can be used to excite an electron in the valence band. Thermal excitation promotes electrons from the valence band to the conduction band, resulting in the formation of an equal number of holes in the valence band. Furthermore, light absorption by

semiconducting materials results in the formation of electron-hole pairs. The magnitude and energy of the absorption process are determined by the semiconductor's band structure[40].

2.5 Mechanism of generating oxidizing species

Heterogeneous photocatalysis is a complicated series of reactions. The oxidizing pathway is still not completely understood. The reaction itself occurs in the adsorbed phase in a classical heterogeneous photocatalytic process, and the overall process can be decomposed into five independent steps: the mass transfer of reactants in liquid phase to catalyst surface, the adsorption of the reactants onto the photon activated catalyst surface i.e. surface activation by photon energy occurs simultaneously in this step[41].

There are two ways in which OH radicals can be formed. As shown in equations 5 and 6, the valence band hole (h^{+}_{VB}) can react with either adsorbed water or adsorbed hydroxyl groups (OH^-) on semiconductor photocatalysts (SC) [42].

$$SC + hv \rightarrow SC\ (e^-_{CB} + h^+_{VB}) \quad (1)$$

$$SC(h^+_{VB}) + H_2O_{ads} \rightarrow SC + HO^{\bullet}_{ads} \quad (2)$$

$$SC(h^+_{VB}) + HO^-_{ads} \rightarrow SC + HO^{\bullet}_{ads} \quad (3)$$

The oxidation potential in equations 1 and 2 must be greater than the upper energy level location of the semiconductor valence band to oxidize hydroxide ions or water. In photocatalysis, oxygen is commonly considered to have a substantial role. As seen in equations 3 and 4, oxygen can capture electrons in the conduction band, forming the superoxide ion $O_2^{\bullet -}$. When these superoxide ions come into contact with hydrogen ions, they create $HO_2^{\bullet -}$

$$SC\ (e^-_{CB}) + O_{2ad} \rightarrow SC + O_2^{\bullet -} \quad (4)$$

$$O^{\bullet -}_2 + H^+ \rightarrow HO_2\cdot \quad (5)$$

The following reaction could also produce H_2O_2 from $H_2^{\bullet}$ species.

$$SC(e^-_{CB}) + O_2^{\bullet -} + H^+ \rightarrow H_2O_2 + SC \quad (6)$$

The photogenerated hydrogen peroxide is further decomposed to produce hydroxyl radicals.

$$H_2O_2 + hv \rightarrow 2OH^{\bullet} \quad (7)$$

$$H_2O_2 + 0^-_2 \rightarrow OH^{\bullet} + O_2 + HO^- \quad (8)$$

$$H_2O_2 + SC(e^-_{CB}) \rightarrow OH^{\bullet} + OH^- + SC \quad (9)$$

It should be mentioned that it takes three electrons to produce one hydroxyl radical through the above pathway, but it takes only one hole to produce a hydroxyl radical from adsorbed water or hydroxyl group. Therefore, most of the hydroxyl radicals are generated through-hole reactions. Nonetheless, the presence of electron scavengers (adsorbed oxygen) is critical for extending recombination and ensuring the successful operation of the photocatalysis process. The presence of oxygen prevents the recombination of electron-hole pairs while allowing the formation of superoxide radicals, as shown in equation 6.

However, without the presence of water molecules, highly reactive hydroxyl radicals cannot be formed, thereby impeding the photodegradation of liquid-phase organics. According to a few reports, the photocatalytic reaction cannot occur in the absence of water molecules. The primary oxidant for the degradation of organic pollutants is the hydroxyl radical produced by the oxidation of adsorbed water where it is adsorbed as OH. Organic compounds are oxidized via a series of free radical reactions, which generate a large number of intermediates. Which then undergo oxidative cleavage, resulting in the formation of carbon dioxide, water, and inorganic ions. When the reduction of oxygen and the oxidation of pollutants do not occur simultaneously. In the photocatalytic degradation of pollutants, there is an electron accumulation in the CB, causing an increase in the rate of recombination of e^- and h^+[43].

2.6. Photolysis and its requirement for photocatalysis

The semiconductor's band edge position is one of the most important and useful parameters to consider when using it as a photocatalyst. The band positions or flat band potentials are useful because they indicate the thermodynamic limits for the photoreactions that can be performed with charge carriers[44]. The semiconductor's band energy positions and the adsorbed species' redox potentials determine a semiconductor's ability to perform photoinduced charge carrier transfer to adsorbed species on its surface. The reduction potential of photoelectrons is determined by the energy level at the bottom of the conduction band. Photo holes' oxidizing ability is determined by the energy level at the top of the valence band, with each value reflecting the system's ability to induce reductions and oxidations, respectively[45]. The flat band potential determines the energy of the two charge carriers at the contact. The proton exchange equilibria and the type of the substance determine this. Conduction band electrons can photo-catalytically reduce adsorbed couples if their redox potentials are higher than the flat band potential of the

conduction band. They can be oxidized by valence band holes if their redox potentials are more negative than the valence band's flat band potential [46]. However, the primary criteria for selecting a good semiconductor photocatalyst for organic compound degradation are the redox potential of the $H_2O/OH^{\bullet}$ ($HO^- = OH^{\bullet} + e^-$, $E° = -2.8$ V) couple lies within the material's bandgap domain and that they are stable over long periods [47]. The following characteristics should be present in an ideal photocatalyst photoactive, capable of utilizing visible and/or near-UV light, biologically and chemically inert, photostable (not prone to photoanodic corrosion), affordable; and non-toxic. Figure 5 shows the slight change in the bulk electronic structure of the semiconductors with pressure and temperature. The pH of the electrolyte used in the study influences the band edge position of the various semiconductors when compared to the redox potentials for the adsorbate[48].

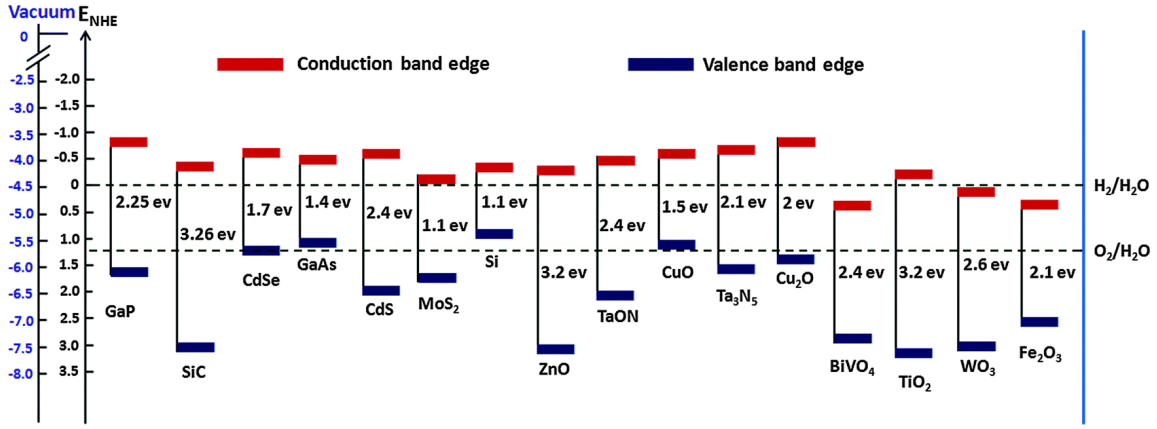

Figure 5. *Band position of commonly used semiconductors in the aqueous electrolyte at pH 1[48].*

In terms of energy utilization (solar or UV light), semiconductors with lower bandgap energy are more desirable. Even though such semiconductors typically have such large bandgaps that they can only absorb UV light. Some of the semiconductors shown in Figure 5 have sufficient band gap energies to be excited by UV or visible light. The redox potentials of the valence and conduction band edges can promote a series of oxidative and reductive reactions. Nonetheless, some of the candidates are not stable in aqueous media over long periods[49].

2.7 Semiconductor reaction

2.7.1 Oxidation reaction

In wastewater treatment, the positive holes formed in the semiconductor's valence band as a result of the electron shift to the conduction band. The light radiation cause oxidization of water that is absorbed to the surface of the semiconductor during the reaction to form hydroxyl radicals. Due to the hydroxide radicals' decomposition power, the formed hydroxide radicals react with the organic matter present in the dyes. If oxygen is present during the process, the intermediate organic molecules and oxygen undergo a radical chain reaction by consuming the dispersed oxygen, and the organic molecules decompose to carbon dioxide and water. Under these conditions, oxidative decomposition occurs as a result of the direct reaction of positive holes and organic compounds [50, 51].

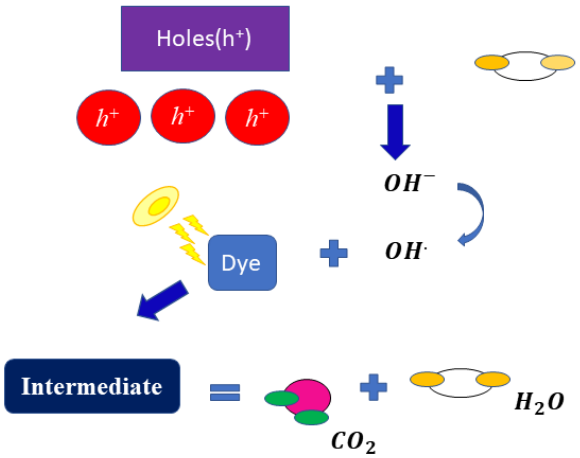

Figure 6. *Schematics representation of oxidation processes.*

2.7.2 Reduction reaction

The reduction reaction occurs when dissolved oxygen combines with the conduction band electron to generate superoxide. The superoxide created in the oxidation reaction are coupled to the intermediate product to yield peroxide or hydrogen peroxide, which is then converted to water[50].

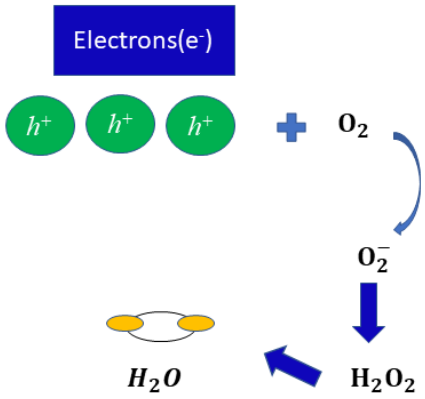

Figure 7. *Schematic representation of reduction reaction.*

2.8 Doping of semiconductors with metal and nonmetals

Nonmetal, metal, and transition metal doping of semiconductors is a straightforward way for improving photocatalytic performance by suppressing charge carrier recombination and increasing the specific area of the semiconductor material. Furthermore, the defect state formed in the semiconductor's bandgap during the doping process enables visible light absorption[52]. Under sub-bandgap irradiation, trapping of valance band VB holes and conduction band (CB) electrons in the defect state to the CB or from the VB to the defect states inhibits rapid charge carrier recombination and enhances interfacial charge transfer[53]. Metal ion doping is the favored doping process because the metal dopant can transfer electrons and lower the semiconductor's bandgap energy level. They are also activated in the presence of a light source, producing electrons. Metal ion doping is the favored doping technique since it can transfer electrons and lower the semiconductor's bandgap energy level. They also become active in the presence of a light source, producing electrons[54].

2.9 Doping with rare earth and transition metals

Doping rare earth and transition metal elements in CuO causes the bandgap to shrink, and absorption in the visible region results in increased optical activity. This facilitates the concentration of contaminating molecules on the CuO surface and improves CuO NPs' light sensitivity. Thus, to improve charge carrier transference in CuO NPs, a growth procedure, i.e., doping method, is used, which aids in organic pollutant photodegradation. Because of the following factors, adding dopants to a pure CuO nanostructure improves photodegradation efficiency by improved electrical conduction, Enlarged surface area, High dopant concentration

increases degradation efficacy, Temperature variations modify degradation capability, and Strong recyclability[40].

2.10 Cu based photocatalyst materials

Cupric oxide (CuO) is a p-type semiconductor with a narrow bandgap (1.2–2.0 eV) that serves as the foundation for many high-temperature superconductors and giant magnetoresistance materials[55]. CuO monoclinic crystal structure has excellent physical and chemical properties, including large surface areas, correct redox potential, good electrochemical activity, super thermal conductivity, and good solution stability[56]. CuO is made up of 3d and O2p shells that are filled by CB and VB edges and have a reduced bandgap, resulting in maximum ROS formation and visible light absorption even in the infrared region [57]. CuO photocatalyst with 1.7 eV bandgap has CB and VB potentials of 0.46 V and 2.16 V, respectively. They are higher than conventional redox potential and suitable for the release of $^{\bullet}OH$ and $^{\bullet}O_2^-$ radicals, which are necessary for photodegradation[58]. CuO has been studied extensively for decades to gain a better knowledge of its physical features, which include crystal structure, and electrical, optical, and magnetic properties. CuO is a prototype material because it has a tenorite monoclinic crystalline structure with low symmetry and generic formula units/unit cells [59, 60]. Cu atom has four coordination numbers for magnetic structure, four O atoms are coupled to Cu in a (110) plane of square planar configuration, and each O atom is surrounded by four Cu in a somewhat distorted tetrahedron form[61]. Because 1D nanostructure materials have more grain boundaries and exposed active crystal planes, they have higher surface-to-volume ratios, which means better photocatalysis activity[62].

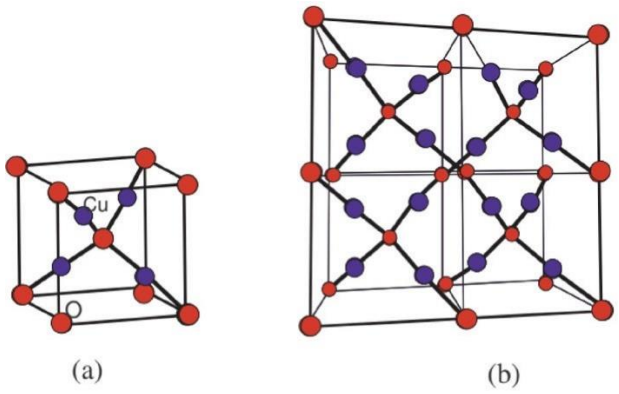

Figure 8. *Copper(I) oxide. (a) Unit cell (b) Three-dimensional crystal lattices of Cu and O are shown in blue and red spheres, respectively[62].*

The study was conducted without adding any surfactants, a cost-effective and environmentally friendly method for the synthesized samples confirmed by the XRD result. ZnO and CuO nanoparticles employing ferulago angulata (schlecht) boiss extract as a mild and non-toxic reducing agent and efficient stabilizer. Secondary metabolites, which are abundant in plants, play an important role in nanoparticle formation. The nanoparticles were discovered in CuO NPs using FESEM. CuO NPs have a shell-like sheet structure with varying surface area and dispersion. The FESEM images of ZnO NPs, were spheroid in shape and polydisperse, with average particle sizes ranging from 32 to 36 nm. The biosynthesized ZnO NPs and CuO NPs were found to be crystalline, with higher purity and a particle size of 44 nm, according to X-ray diffraction data. According to this research, ZnO NPs have a better photocatalytic degradation capacity than CuO NPs[63].

2.11 CuO based heterostructure construction for pollutant degradation

Due to quick charge recombination, bare CuO is ineffective for pollutant degradation; consequently, it is necessary to improve its photodegradation efficacy and make it an efficient photocatalyst. Heterojunction production occurs when two different semiconductors with suitable bandgap alignment come together to improve electron transport by lowering photogenerated charge carrier recombination rates. The most promising method for improving the photocatalytic performance of photocatalysts is this one[64, 65]. CuO photocatalysts have a lower bandgap, which leads to electron-hole pairs (EHP) recombination and so have poor photodegradation efficacy. Based on the bandgap edges of the composite photocatalyst, the approach is divided into four categories the first is In a type-I heterojunction, as shown in Figure 9 (a) the (photosystem) PS-VB I's and CB positions are lower and more significant than the VB and CB of neighboring PS-II, causing photoexcited holes and electrons from PS-I to migrate to the negative VB and CB of PS-II for charge separation. The second is a type-II system, as shown in Figure 9 (b)VB and CB of PS-I are higher than VB and CB of PS-II, allowing electrons to easily migrate from CB of PS-I to PS-II with reduced reduction potential while holes migrate from VB of PS-II to PS-I with reduced oxidation potential, resulting in spatial electron-hole separation. The third is Charge carriers migrate in a type-III as shown in Figure 9 (c) heterojunction in the same way they do in a type-II heterojunction, but the band edges are further set off, resulting in no EHP transfer or separation. The fourth is the Z-scheme is a subset of heterojunction construction that is used to mitigate the disadvantages of heterojunction systems

with lower redox potentials[66]. Electrons/holes were collected on different PSs, resulting in charge carrier separation in space. This cutting-edge method allows photogenerated charge carriers to migrate across short distances without recombination to active areas on the photocatalyst surface as shown in Figure 9 (d). Beyond all three heterojunction systems, type-II heterojunction provides optimum band positions for efficient charge carrier separation leading to enhanced photocatalytic activity. The build-in potential at the interface of semiconductors can enhance the transference and separation of photogenerated EHP. As a result of its superior photocatalytic performance due to reduced EHP recombination which provides efficient charge carriers for reactive radical formation. This is considered the most prominent composite photocatalytic system among all heterojunctions[67].

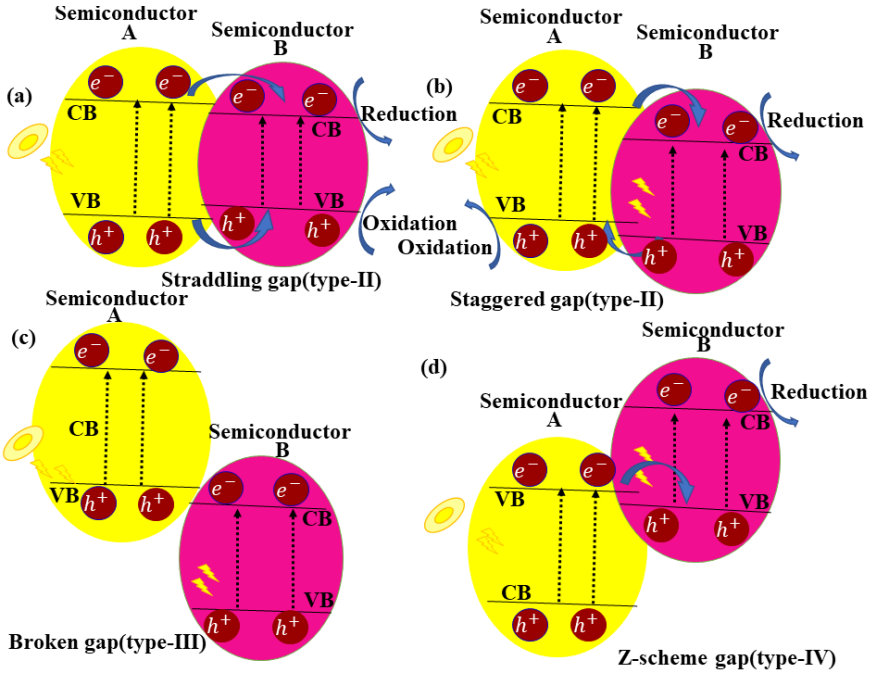

Figure 9. *The mechanism for photocatalyst heterojunction.*

2.11.1 CuO based Type-II binary heterostructure photocatalyst

An excellent structural design for enhancing photocatalytic activity is a heterojunction of two distinct semiconductors. The heterostructure is a term used to describe a variety of various heterojunctions. Two PS used in heterojunction construction must have discrete band gaps with reduced band energy in the visible range for photocatalytic activity. For the degradation of MB contaminants in high salinity wastewater, Li and colleagues created CuO/CeO_2 heterostructure. The photodegradation efficiency of CuO/CeO_2 nanocomposite for methyl blue (MB)

degradation was enhanced from 18 to 33.74 % and was mainly due to the bombardment of ·OH radicals. More than 80% of MB was forcefully removed from wastewater, having 5~80 g/L NaCl in the 2.11~9.02 pH range[68].

They studied by using the production of $CuBi_2O_4$/CuO heterostructure in the shape of nanocolumns with a small plate-like nanoparticle (diameter as small as 2μm) continuously spread over the surface was confirmed by field emission scanning electron microscopy (FESEM) data. Due to successful charge separation under the visible light range with 2.1% apparent quantum yield (AQY= 540 nm), the constructed heterojunction displayed excellent photocatalytic activity with 98 percent and 36 percent removal of MB deterioration and MTZ, respectively. The photodegradation efficiency of $CuBi_2O_4$/CuO heterojunctions was investigated by degrading MB dye and metronidazole under simulated solar light and visible light irradiation (MTZ)[69].

They studied a photocatalyst based on CuO/SiO_2 they developed and tested for methylene blue degradation in an aqueous medium. The photocatalyst was made using a copper salt calcination technique in the presence of silica. CuO impregnation of the silica surface, as well as discontinuity and roughness, were visible in SEM micrographs of CuO/SiO_2 photocatalyst but the pure silica surface. Using the BET technique, the specific surface area of CuO/ SiO_2 was 284 m^2 g^{-1}. When compared to other conditions, tests of methylene blue degradation revealed that CuO/SiO_2, in the presence of ultraviolet radiation and hydrogen peroxide, enhanced the rate of methylene blue degradation significantly. CuO/SiO_2 requires more research to improve its activity in the presence of visible light, as this is a critical aspect of achieving long-term economic development[70].

The study on composites of ZnO/CuO a popular method for water purification for degradation of organic pollutants. They examined the influence of copper acetate concentration on nanocomposites' functional qualities. The electronic states of Zn and Cu revealed a peak shift in X-ray photoelectron spectra analysis. The existence of CuO was confirmed by the presence of uniformly dispersed CuO on the surface of ZnO. The SEM morphology of CuO nanoparticles spread equally on the surface of ZnO nanorods. Under visible light irradiation, the photocatalytic activity of ZnO/CuO composites was higher than pure ZnO[71].

2.12 Synthesis techniques of metal oxide nanomaterials

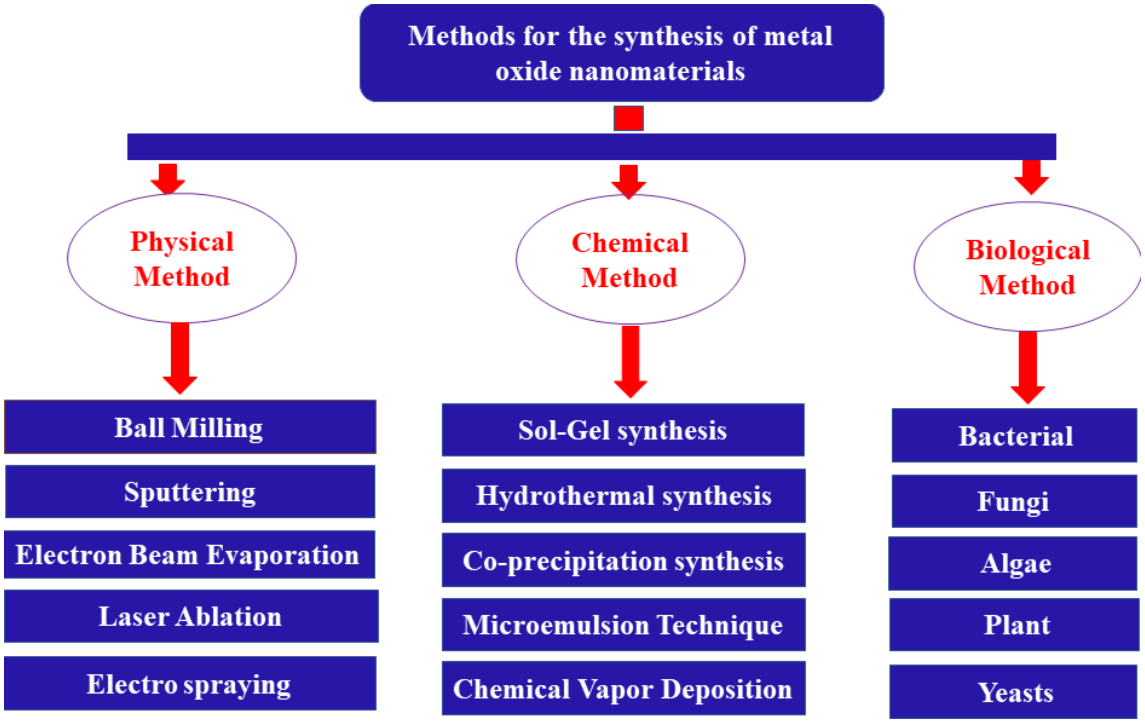

Figure 10. *Schematics of synthesis methods of metal oxide.*

2.12.1 Green Synthesis of Metal NPs

The research and design of nanoparticles employing nontoxic chemicals, renewable materials, environmentally being solvents, and finally, degradable waste products are all part of the green synthesis approach to nanoparticles[72]. From a green chemistry perspective, three crucial phases in the synthesis of nanoparticles are the use of a non-toxic solvent medium, a nontoxic reducing agent, and environmentally friendly stabilizing agents[73].

2.12.2 Copper Oxide Nanoparticles (CuO NPs)

Biogenically synthesized CuO NPs have been shown to be both cost-effective and environmentally begin, and they come in a variety of sizes depending on the plant source. Green-produced CuO NPs have UV absorption bands of 265–285 nm (strong band) and 670 nm (weak band), which correspond to the Cu metal interband transition of core electrons and the CuO band edge transition, respectively[74].

Biogenic synthesis study of nanoparticles utilizing natural herb extracts (*Azadirachta*) that has a wide range of applications due to its low cost, non-toxic, environmentally friendly nature, and ability to switch between physical and chemical functions. They indicated extract modified

CuO, silver doped Azadirachta indicated extract modified CuO, molybdenum doped Azadirachta indicated extract modified CuO, and silver, molybdenum with Azadirachta indicated extract doped CuO nanoparticles they prepared successfully. They calculated from the Xrd result shown below nanoparticles have particle diameters of 25 nm, 19.8 nm, 17.20 nm, 14.57 nm, and 11.23 nm, respectively. SEM images of nanoparticles as they observed, these nanoparticles are mostly made up of nanoflakes, and their size decreases when made using plant extracts. Under solar light irradiation, the solar photocatalytic action of nanoparticles was measured using MB dye. In a pseudo-first-order kinetics model (1.704×10^{-2} s^{-1}), the photocatalyst may break down and satisfactorily mineralize MB dye in a short illumination time of 180 min. The inhibition of electron-hole recombination by secondary metabolites in the plant extract, Ag and Mo in CuO, results in increased photocatalytic activity of 99% [75].

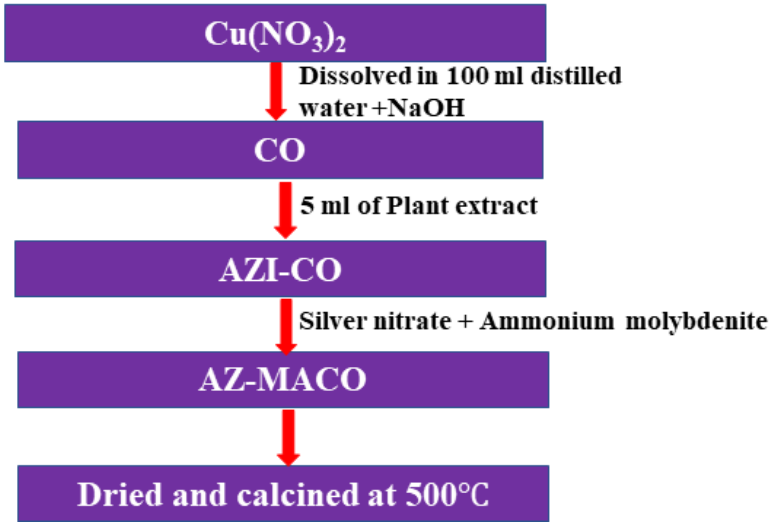

Figure 11. *Biogenic synthesis of nanoparticles.*

2.12.3 Iron Oxide Nanoparticles (Fe_2O_3 NPs)

Fe_2O_3 NPs another transition metal oxide NP that has been studied because of their impact on the creation of materials used in magnetism, catalysis, sensors, optics, and biomedicine due to their electrical, magnetic, optical, electronic, and catalytic capabilities. Hematite (α-Fe_2O_3), bixbyite (β-Fe_2O_3), maghemite (γ-Fe_2O_3), ε-Fe_2O_3, magnetite (Fe_3O_4), and wurtzite are some of the minerals that include it (Fe-O). Because of its tiny size and huge surface area, hematite is the most thermodynamically stable of the three. Due to its remarkable qualities of low cost, simple production, environmental friendliness, non-toxicity, strong corrosion-resistance, and

excellent chemical stability, hematite phase iron oxide (α-Fe_2O_3) is also considered to be one of the most important semiconductors photocatalysts in recent times[76].

Moringa Oleifera leaf extracts were employed to produce hematite nanoparticles, according to the study. Phytochemicals, which act as stabilizing, capping, and surfactants, are made from plant extracts. According to current research, green hematite nanopowder is environmentally friendly, takes little time to prepare, is an affordable and promising candidate material for electromagnetic devices and ferromagnet manufacturing, and can be used as a photocatalyst in water treatment applications without the use of additives (H_2O_2)[77].

The study on the extract of Guava (Psidium guajava) leaves to perform abiogenic production of α-Fe_2O_3. The average diameter of α-Fe_2O_3 nanoparticles is around 34 nm. Absorption measurements of the material indicate four absorption bands at 347 nm, 543 nm, 652 nm, and 849 nm, ranging from UV to near IR. The presence of indirect and direct bandgap energies of α-Fe_2O_3 is demonstrated by UV-Visible absorption. Due to band edge emission, the PL spectra of nanoparticle clusters excited at 460 nm exhibits an emission band at 688 nm. At room temperature, the VSM investigation revealed a hysteresis loop, indicating the synthesized sample's mild ferromagnetic character. Shape anisotropy is responsible for the observed high value of the coercive magnetic field. The synthesized material is shown to be an excellent contender for improving the thermal conductivity of common base fluids such as water and ethylene glycol. Hematite nanoparticles' antibacterial activity against Gram-positive and Gram-negative bacteria has also been demonstrated[78].

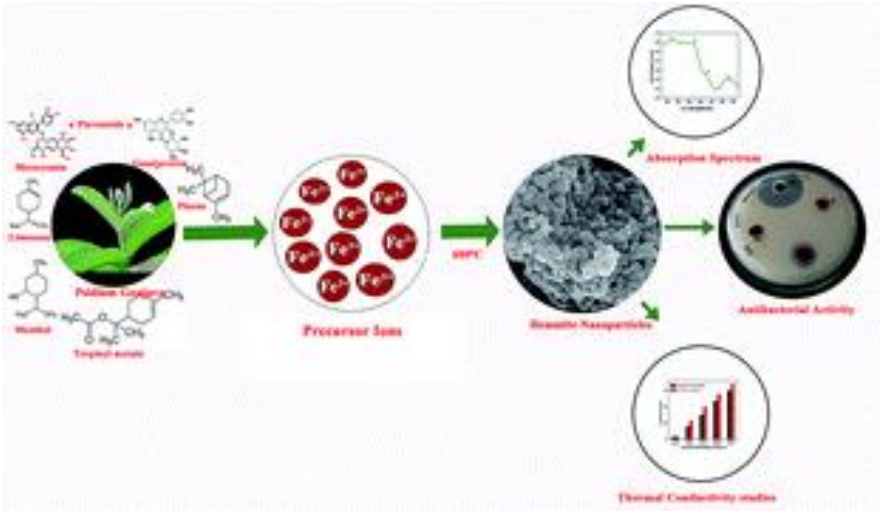

Figure 12. *Morphology, Uv, photocatalytic and antibacterial properties of* Fe_2O_3*[78].*

2.12.4 Background of *Acmella Ciliata (*Kunth.) (*Asteraceae*)

Acmella Ciliate is a medicinal plant of African origin, a native plant of tropical and subtropical regions of the world, primarily Ethiopia, India, and South America. It is commonly referred to as the toothache plant since it relieves toothache pain and stimulates saliva production. Various extracts and active metabolites derived from different sections of this plant have pharmacological properties. It has antimicrobial, immunomodulatory, and anti-histamine properties that help with heartburn, gastrointestinal issues, gastritis control, headache, and diarrhea[79]. Saponins, organic acids, reducing sugars, phenols, tannins, alkaloids, Flavonoids, Anthraquinones, and Triterpenes were all detected by phytochemical test[80]. The high antioxidant potential of citric acid is well known, indicating that Acmella Ciliata is a prospective source of this chemical. The same functions are given to phenolic chemicals, which are prevalent in many plant species and have antioxidant capacity regardless of class[81]. Fruits, vegetables, and plant-based diets are high in phenolic chemicals, which have been linked to a lower risk of cardiovascular disease, cancer, and other chronic diseases[82]. This connection is explained in part by these compounds' ability to scavenge free radicals and pro-oxidant metals (antioxidant activity)[83].

Figure 13. *Acmella Ciliata (Kunth.) (Asteraceae).*

Table 1. *Biosynthesized metal-doped copper oxide-based Nano-catalysts in the degradation of pollutants in water.*

S. No.	Catalysts	Biogenic source	Particle size(nm)	Morphology of NPs	Activity carried out	Method	Efficieny (%)	Ref.
1	Zn-Doped CuO	Alginate biopolymer	16.05	nanoflowers	MB	Hydrothermal	1.7175 h^{-1}	[84]
2	CuO	Madhuca longifolia	30	spherical	MB			
3	CuO	Banana peel	60	Crystalline spherical	CR	Coprecipitation	90	[85]
4	CuO	glutamic acid	15	2D leaf-like structure	Rose Bengal and MV	microwave irradiation	97.5	[86]
5	CuO	Rhizome extract of Bergenia ciliata	20	Spherical shaped	MB and MR	Coprecipitation	92 85	[87]
6	CuO NPs Ag/CuO NPs	Cyperus pangorei	17–32	spherical shape	Rh-B	co-precipitation	92	[88]
7	CuO Nanostructures	O. sanctum leaves (Tulsi) leaf	250	Flower-Shaped	MB	co-precipitation	90	[89]

8	Ag-Mo/CuO nanoparticles	Azadirachta indica leaf	12	Nanoflakes	MB	co-precipitation	99	[75]
9	CuO/rGO nanocomposite	Terminalia arjuna	0.34	sheet-like	MO	Sol-gel	90	[90]
10	N-doped carbon/CuO-Fe_2O_3	Melamine	300	porous spherical structure	MB	green one-pot annealing	98	[91]
11	ZnO/CuO	Ginkgo leaves	22	spherical	MO	co-precipitation	99	
12	Mg-CuO/Fe_2O_3		-	-	phenol	hydrothermal	84.36	[92]
13	Ni-doped CuO/Fe_2O_3	*Acmella ciliate*	-	-	MB			**[***In this work***]**

To the best of our knowledge, no research work has been conducted on plant-mediated (1-x)2NCO/(x)Fe_2O_3 (x=0.1, 0.2, 0.3, 0.4, and 0.5). This research work cost-effective, economic, and environmentally friendly approach using a plant type *Acmella Ciliata* which is used as a capping/stabilizing agent for the synthesis. Doping Ni on CuO/Fe_2O_3 increases the photolytic activity of the catalyst during the degradation of methylene blue.

CHAPTER THREE

3. Materials, Methods, and Characterizations

3.1 Materials

For this work, Copper Nitrate Hexahydrate (Cu $(NO_3)_2.6H_2O$) (Loba Chem, 96%, India), Nickel Nitrate Hexahydrate ((Ni $(NO_3)_2.6H_2O$)) (Loba Chem 98%, India), Iron Nitrate Hexahydrate (Fe $(NO_3)_2.6H_2O$) (Loba Chem, 97%, India), Sodium Hydroxide (NaOH) (Loba chem, 95%, New Delhi) and Methylene Blue (Carelabmed Chem, India). For all syntheses, distilled water and ethanol were employed. The filter paper was employed for filtration of Acmella Ciliate plant leaves obtained from Arbaminch, S/N/N/P/R, Ethiopia.

3.2 Methods

3.2.1 Preparation of plant extract

First, the leaf of *Acmella Ciliate* plant (2 g fresh leaves) was washed with deionized water several times to remove unwanted materials incorporated into the leaf. The washed leaf was mixed into 100 ml of deionized water. Then the mixture was heated and stirred at 70 ºC for 30 min then the mixture was placed at room temperature until cool down. After the mixture was cold down, the solution was faltered by filter paper. The obtained solution was stored at 4 ºC for further studies[88].

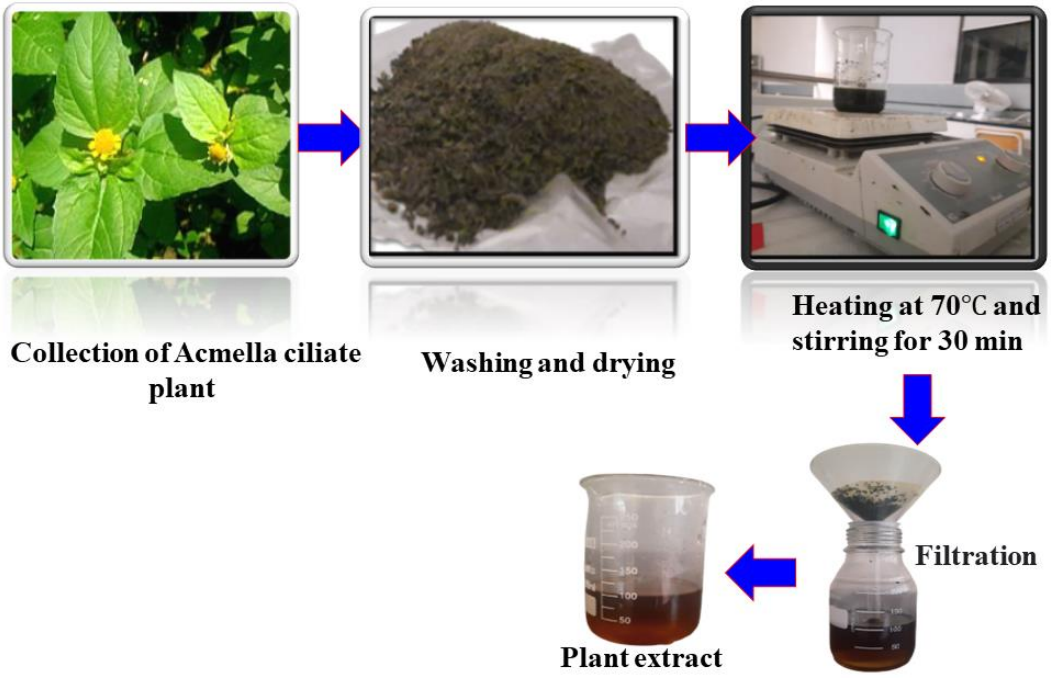

Figure 14. *Schematics plant extraction process.*

3.2.2 Biosynthesis of CuO

CuO was prepared in 100 ml of a plant extract with a 1 M Cu $(NO_3)_2.3H_2O$ the obtained solution was stirred for 30 min at 70 ºC. Freshly prepared 0.4 M NaOH was dissolved into 100 ml distilled water and added drop wisely into the solution until the pH of the solution reaches 12. The color of the solution changed from light green to dark brownish. The obtained solution was stirred further for 2 h. After 2 h, the solution precipitated at room temperature by leaving for 12 h. The precipitated solution was rinsed three times with deionized water and ethanol before being dried at 100 ℃ for 5 h. Finally, the resulting powder was calcined at 400 ºC for 2 h named as p-CuO[89]. For comparison, CuO was synthesized by a chemical synthesis route following all the above procedures except the utilization of the plant extract. To enhance the photocatalytic activities of copper oxide. Plant extracted CuO was doped with different doping concentrations. A similar procedure was used to synthesize doped copper oxide by adding different percentages as shown in Table 2 [93].

Table 2. *Different Percentage of Nickel and Copper oxide with their naming.*

Name of Samples	Percentage of composition
1NCO	1% Ni and 99% CuO
2NCO	2% Ni and 98% CuO
3NCO	3% Ni and 97% CuO
4NCO	4% Ni and 96% CuO

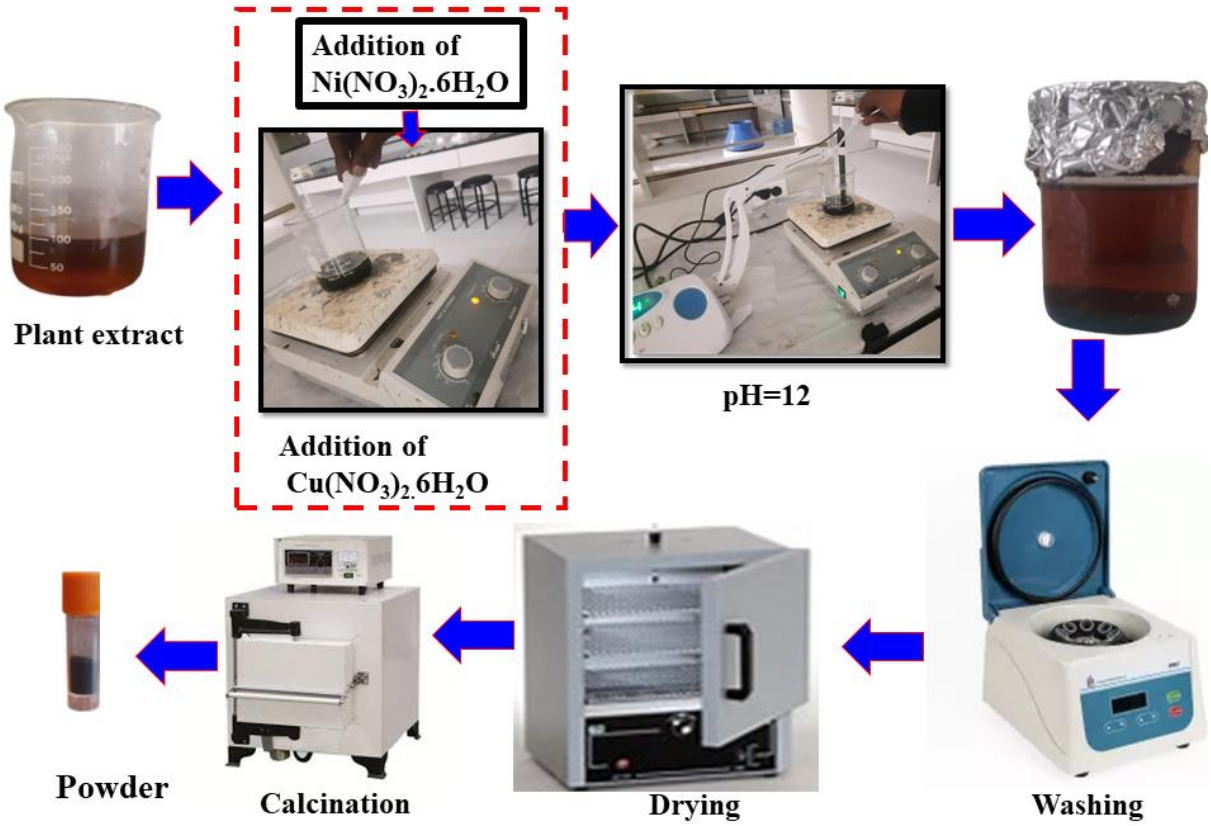

Figure 15. *Schematics of CuO, 1NCO, 2NCO, 3NCO, and 4NCO Synthesis.*

3.2.4 Biosynthesis of Fe_2O_3

Fe $(NO_3)_2.6H_2O$ and NaOH were used for synthesizing Fe_2O_3 powder. Typically, 0.1 M of iron nitrate was dissolved into 100 ml of plant extract, and similarly, 0.2 M of sodium hydroxide was dissolved into 100 ml of deionized water. The prepared solution was added drop wisely until the pH of the solution reaches 12. The mixture was then stirred for another 2 h at 50 °C. The mixture was then allowed to precipitate for 12 h before being rinsed with ethanol and deionized water and dried for 6 h at 100 °C. Finally, the powder was calcined for 3 h at 550 °C to obtain Fe_2O_3 power[94].

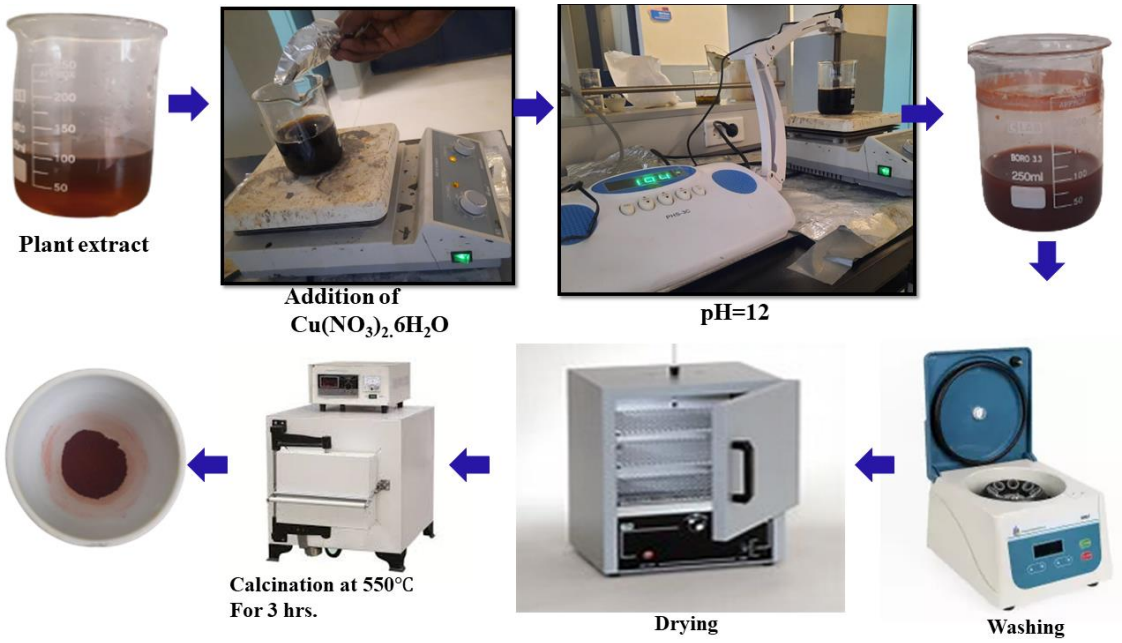

Figure 16. *Schematics of Fe_2O_3 Biosynthesis.*

3.2.5 Synthesis of 2NCO/FO

To synthesize composite 2NCO/10FO, 2NCO/20FO, 2NCO/30FO, 2NCO/40FO, and 2NCO /50FO. The 2NCO (90%, 80%, 70%, 60%) and Fe_2O_3 (10%, 20% 30%, 40%, 50%) dissolved respectively into 100 ml of plant extract. For different, each prepared composite 0.2 M NaOH solution was added drop wisely until the pH of the solution reaches 12 at 50 °C with a continuous stirring for 2 h. Then the mixture was placed for 12 h to get the mixture precipitated. After the mixture gate precipitated the precipitate was washed with ethanol and deionized water followed by drying at 100 ºC for 12 h. Finally, the obtained powders were calcined by determined TGA result at 550 ºC for 3 h[95].

Table 3. *Percent of the composition of Nickel doped Copper Oxide and Iron oxide with its naming.*

Name of Samples	Percentage of composition
2NCO/10FO	2NCO (90%)/Fe_2O_3(10%)
2NCO/20FO	2NCO (80%)/F_2O_3(20%)
2NCO/30FO	2NCO (70%)/Fe_2O_3(30%)
2NCO/40FO	2NCO (60%)/Fe_2O_3(40%)
2NCO/50FO	2NCO (50%)/Fe_2O_3(50%)

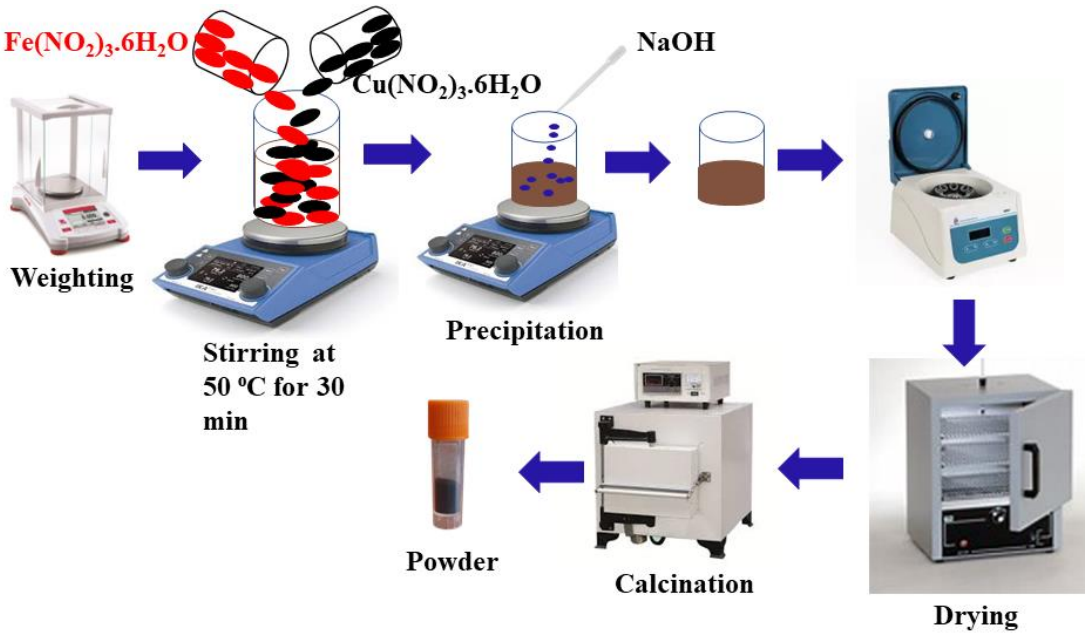

Figure 17. *Schematics of synthesis composite 2NCO/10FO, 2NCO/20FO,2NCO/30FO, 2NCO/40FO, and 2NCO/50FO.*

3.3 Characterizations

The prepared CuO, *p*-CuO, Fe_2O_3, 1NCO, 2NCO, 3NCO, 4NCO 2NCO/10FO, 2NCO/20FO, 2NCO/30FO, 2NCO/40FO, and 2NCO/50FO were studied by various technique. The phase purity was examined using XRD (XRD-700, Shimadzu, South Korea) at copper Kα radiation (λCuKa = 1.5418 Å), with a scan speed of 4 (deg/min), voltage (40 kV), current (30 mA), and scanning range (4-80°). TGA-DTA (DTG-60H, Shimadzu, South Korea) was used to study the thermal stability of the 2NCO/10, 2NCO/30FO, and 2NCO/40FO from 20 to 900 °C under both in air and in an argon atmosphere at a scanning rate of 10 ℃/min from room temperature to 900 ℃, using α-Al_2O_3 as reference. SEM (COXIEM-30 (Shimadzu, South Korea)) was also used to examine the microstructure, morphologies, and elemental content of the samples CuO, *p*-CuO, Fe_2O_3, and 2NCO /40FO. FTIR spectra with a wave number range of 500-4000 cm^{-1} were collected using an FTIR (Quanta chrome Nova Win, India) spectrophotometer to identify functional groups on the adsorbent surface. BET (V-Sorb 2800S, china) strives to explain the physical adsorption of gas molecules on a solid surface and provides the foundation for a key analysis approach for determining the specific surface area of CuO, p-CuO, and Fe_2O_3. The visible light absorbance property of CuO, Fe_2O_3, 1NCO, 2NCO, 3NCO, 4NCO, 2NCO/10FO, 2NCO/20FO, 2NCO/30FO, 2NCO/40FO, and 2NCO/50FO from Tauc plot optical band gap of CuO, 2NCO, Fe_2O_3 and 2NCO/40FO were estimated using (UV-3600Plus). Spontaneous

emission of light from an under optical excitation of CuO, Fe_2O_3, 2NCO, and 2NCO/40FO was determined by PL. To explore different locations and excitation concentrations in the sample, the excitation energy and intensity are chosen. The interface charge separation determined the efficiency of CuO, Fe_2O_3, 2NCO, and 2NCO/40FO EIS (Biologic Sp-300, Korea). After the photocatalytic experiment, the absorbance of the MB dye was measured using a UV-visible spectroscope (UV-3600Plus, Korea). For all synthesis, the pH of the solution is adjusted using pH mater (PHS-3C, China).

3.4 Photocatalytic activity study

The photocatalytic performance of the synthesized samples was tested using visible light (a 150-Watt Halogen lamp). The 25 mg of catalyst dissolved into 100 ml of 10 parts per million (ppm) MB solution concentration. As shown in Figure 18 the solution was stirred in the dark for around 30 min to achieve adsorption-desorption equilibrium between a catalyst and a contaminant and a 6 ml solution was taken. Following the development of equilibrium, the light was irradiated into the suspension as it was continually stirred, and 6 ml of solution was taken for analysis up to 120 min. Finally, residual pollutant concentrations were detected using UV-visible spectroscopy, and the concentration (C_t) was calculated from the absorbance against the wavelength plot using the Beer-Lambert rule, as shown in equation 10 below.

$$\mathbf{A = \varepsilon b C_t} \tag{10}$$

Where A denotes absorbance, ε denotes absorbtivity, and C_t is the MB concentration after time t.

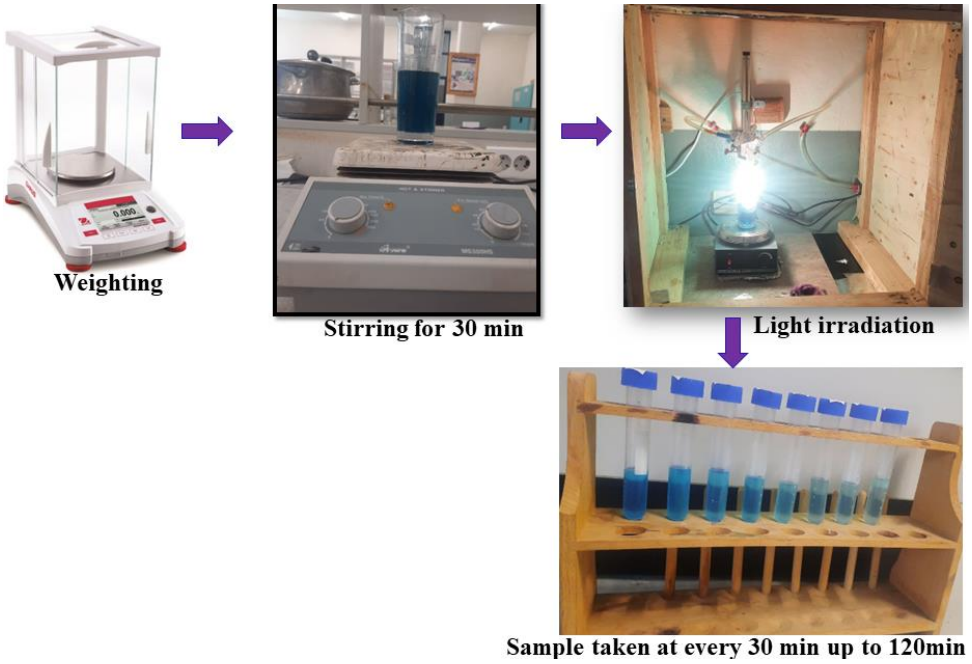

Figure 18. *Schematics of photolytic process.*

CHAPTER FOUR

4. Results and Discussions

4.1 XRD analysis

Figures 19 1(a) and (b) illustrate the XRD pattern of CuO and *p*-CuO confirming the synthesized individual oxides exhibited a single phase. The diffraction peaks at 2θ of 32.51º, 35.56º, 38.92º, 46.47º, 48.84º, 53.68º, 58.4º, 61.6º, 66.3º, 68.16º, 72.46º and 75.26º were correspond to (110), (002), (111), (-112), (-202), (020), (-113), (-311), (31-1), (220), (311) and (004) crystallographic planes, respectively. Shows a cubic crystal structure with a space group of *C2/c* in agreement with JCPDS Card No: 48-1548[96]. The plant extract CuO exhibits similar diffraction peaks and crystallographic planes. In the XRD patterns of Fe_2O_3, as shown in Figure 19 1(c) the diffraction peaks at 2θ 24.14º, 33.28º, 35. 62º, 40.95º, 49.56º, 54.03º, 62.48º, 64.06º, 71.82º, 75.26º, and 77.26º corresponding to (012), (104), (110), (113), (024), (116), (018), (214), (300), (1010) and (220) planes respectively. Fe_2O_3 contains a tetragonal crystal structure with space group *R-3c* the result observed was in close agreement with JCPD card No: 33-664[97].

The XRD patterns of Figure 19 2) (a) *p*-CuO (b) 1NCO, (c) 2NCO, (d) 3NCO, and (e) 4NCO show that no other extra impurities exist for the doping concentration of Ni with 1, 2, 3, and 4% containing a cubic crystal structure. Because of the substitution by similar ionic radii of Ni^{2+} (0.69 Å) with Cu^{2+} (0.73 Å) sites in their monoclinic structure. Moreover, the addition of Ni dopant in the CuO lattice did not alter the lattice and but a small shift occurs in the 2θ values as shown in the inset of the XRD. The reduction in crystallite size of CuO is responsible for the XRD widening. Furthermore, there is no noticeable change in peak location, and the peaks are found to be fairly sharp and strong, implying that the produced powders have high crystallinity. Using the Debye–Scherrer equation, the crystallite size was determined by measuring the full width at half-maximum (FWHM) of the most intense diffraction peak using equation 13[98].

$$D=\frac{k\lambda}{\beta cos\,\theta} \qquad \textbf{(11)}$$

Where is the half maximum intensity (FWHM) of the observed diffraction peak, K is the Scherrer constant 0.9, and is the x-ray wavelength (Cuk radiation, = 0.154 nm). The crystallinity of bare CuO, 1NiCO, 2NCO, 3NCO, and 4NCO is 18.53, 7.67, 8.63, 9.51, and 7.76 nm, respectively. With increasing Ni doping concentrations, the peak intensity declines linearly as

the FWHM increases, indicating crystallinity degeneration of the CuO. The Ni ions move inside the CuO lattice and take up residence in the vacancy. The lattice distortion is caused by the charge imbalance and ionic radius mismatch between Cu and Ni ions. CuO crystallization quality will be affected even more[99].

The thermal property of composite studied 2NCO/10FO, 2NCO/30FO, and 2NCO/50FO by TGA the result show that the synthesized composites are stable at 550 ºC from this result all synthesized composites are stable at this temperature. These composites 2NCO/10FO, 2NCO/20FO, 2NCO/30FO, 2NCO/40FO, and 2NCO/50FO are explained by XRD patterns as shown in Figure 19 3(a)-(g). The diffraction main peaks are at 2θ of 35.5º, 38.7º, 48.7º, 58.3º, 61.6, 66.2º, and 68.2º correspond to (-111), (111), (-202), (202), (-113), (-311), and (200) crystallographic planes, respectively the result well-matched with standard CuO JCPDS card No: 48-1548[100]. The XRD pattern also presented intense diffraction peaks at 2θ of 24.1º, 33.1º, 40.9º, 49.4º, 54.0º, 62.4º, and 64.0º correspond to the (012), (104), (113), (024), (116), (214) and (300) crystallographic planes, respectively the result well-matched with standard Fe_2O_3 JCPDS card No: 33-664[92].

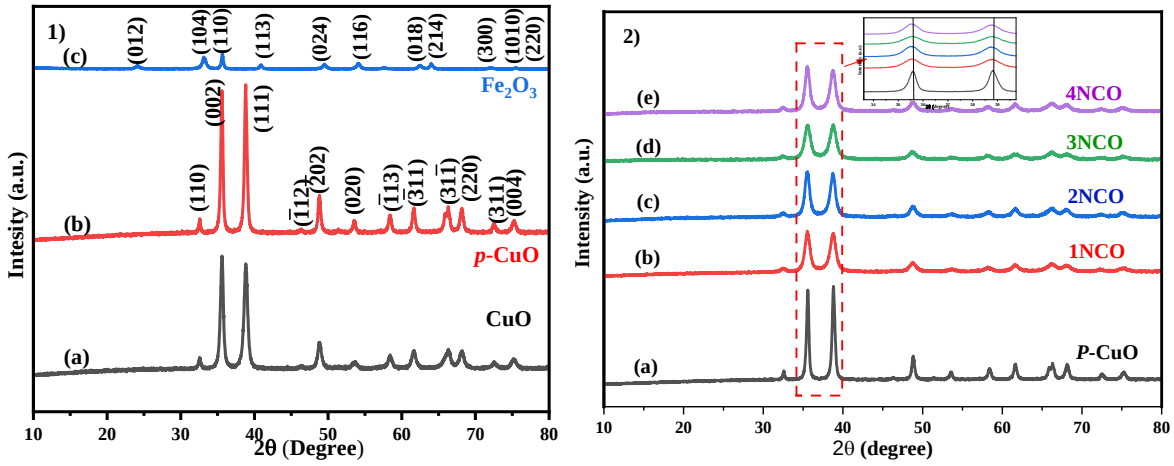

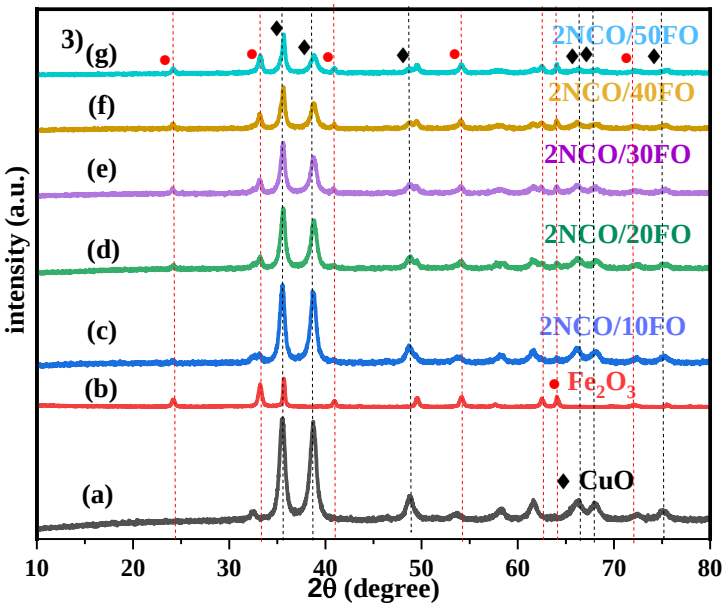

Figure 19. *XRD result of 1) (a) CuO, (b) P-CuO, (c)Fe_2O_3, 2) (a) p-CuO, (b) 1NCO, (c) 2NCO, (d) 3NCO, and (e) 4NCO; 3) (a)Cuo, (b)Fe_2O_3, (c)2NCO/10FO, (d) 2NCO/20FO, (e) 2NCO/30FO, (f) 2NCO/40FO and (g) 2NCO/50FO.*

4.2 Thermal analysis

Figures 20 (a), (b), and (c) shows the TGA-DTA curves of composites 2NCO/10FO, 2NCO/30FO, and 2NCO/40FO. The curve has three peaks of weight loss, namely α, β, and γ decomposition peaks. The first endothermic peak (α region) for composites 2NCO/10FO, 2NCO/30FO, and 2NCO/40FO at a temperature around 121 ºC, with a weight loss of around 2.67, 6.43, and 7.51% respectively. This was due to the evaporation of residual water molecules adsorbed on the surface of the catalyst [101, 102]. At a temperature around 300 ºC, the second step (β region) occurred, representing the evolution of crystallization water, hydroxides, and residual nitrates decompose within these temperature ranges with weight loss of around 5.85, 10.77, and 13.03% for 2NCO/10FO, 2NCO/30FO, and 2NCO/40FO, respectively. In the third step (γ region) a pronounced endothermic peak was observed at about 300 to 550 ºC corresponding to the thermal decomposition of Cu $(OH)_2$ equation 12 and Fe $(OH)_3$ equation 13, forming CuO, and Fe_2O_3 respectively. With the corresponding weight loss of about 6.70, 16, and 14% respectively[103].

$$Cu\ (OH)_2 \rightarrow CuO + H_2O \quad (12)$$

$$2Fe\ (OH)_3 \rightarrow Fe_2O_3 + 3H_2O \quad (13)$$

As a result, there is no significant weight loss from the sample above 550 °C, which could be the point at which the 2NCO/FO begins to form, and the calcination temperatures were limited to above 550 °C to observe the evolution composite of CuO and Fe_2O_3, and the calcination temperatures were limited to above 550 °C to observe the evolution composite of CuO and Fe_2O_3. This demonstrates that the composite of 2NCO/10FO, 2NCO/20FO, 2NCO/30FO, 2NCO/40FO, and 2NCO/50FO was stable and calcined at a temperature of 550 °C.

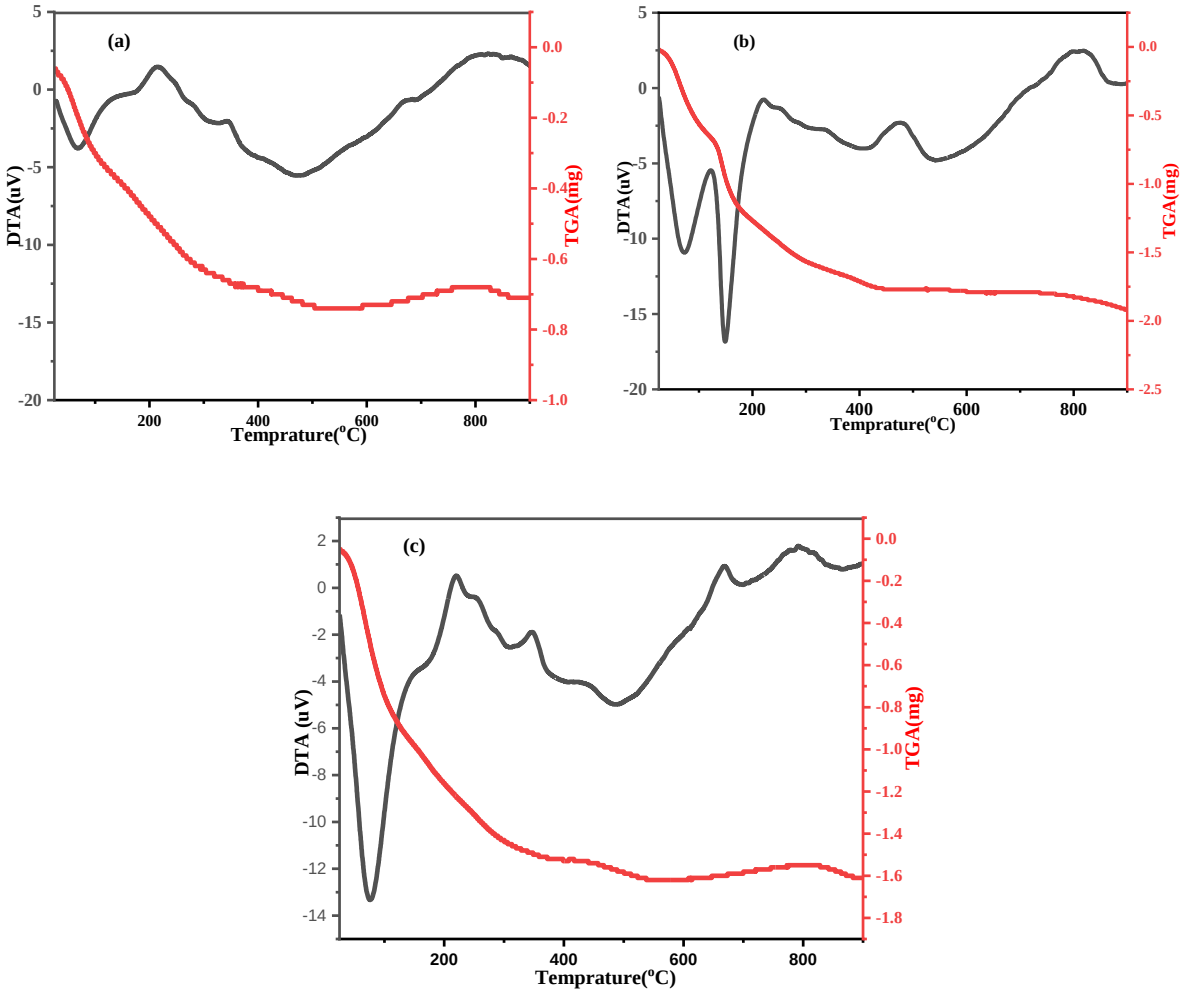

Figure 20. *Thermogravimetric analysis of a) 2NCO/10FO, b) 2NCO/30FO,and C) 2NCO/50FO.*

4.3 FTIR Analysis

The functional groups and chemical structures of Acimella plant powder CuO, Fe_2O_3, p-CuO, and 2NCO/40FO were identified by measuring the FTIR spectra as shown in Figure 21. The broad peak centered at 3436 cm^{-1} corresponds to the stretching vibration of O-H. It manifests

as a broadening of peaks corresponding to O-H covalent bonds, indicating that bond lengths of O-H covalent bonds have increased due to their involvement in hydrogen bonding. The weak peak at 1721 cm^{-1} was attributed to the C=O stretching of COOH groups. The IR band around 1597.29 cm^{-1} can be assigned to aromatic bending of alkene group (C=C) and stretching vibration of epoxy (C-O) groups[104]. The sharp peak at 1342.3 cm^{-1} is attributed to the deformation vibration of the C-H band of the alkane (CH_3 and CH_2) group. The absorption peak at 1038.0 cm^{-1} stretching vibrations of the C–O group of primary and secondary alcohols (C–O). The peak at 875 cm^{-1} is due to C-H stretching vibration and the strong band below 700 cm^{-1} is assigned to Fe-O stretching mode. The peaks positioned around 647.626 and 520 cm^{-1} correspond to the characteristic stretching vibrations of the Cu-O bond in the monoclinic CuO NPs. The characteristic absorption bands of the sample at 555 cm^{-1} are assigned to iron oxide stretching and the bands around 560 cm^{-1} correspond to the Fe-O stretching mode of the Fe_2O_3 phase and the band around 464cm^{-1} was attributed to the lattice mode of Fe-O lattice[105]. The other peaks observed in the spectra were due to stabilizers and hydroxyls adsorbed on the surface of oxide[106]. At 446 cm^{-1} can be assigned to the bending vibration mode of Fe_2O_3[107]. The direction and peaks around 439 and 445 cm^{-1} were due to Cu-O stretching mode[108].

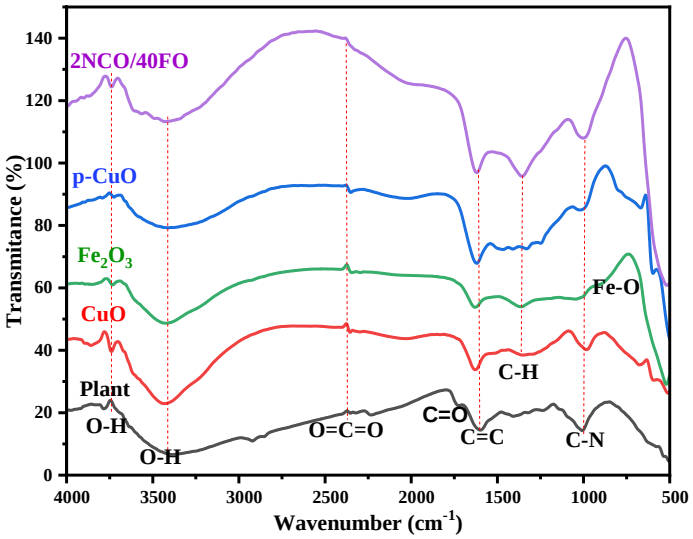

Figure 21. *FTIR spectra of Acimella plant, CuO, Fe_2O_3, p-CuO, and 2NCO/40FO.*

4.4 Morphological Analysis

The morphology of CuO, *P*-CuO, Fe_2O_3 and 2NCO/40FO samples were examined using a scanning electron microscope (SEM). The SEM results are presented in Figure 22 (a) CuO, (b)

p-CuO, and (c) Fe_2O_3. The result shows that the catalysts can create agglomerates of closely packed and even fused particles, which can blind or block accessibility to catalyst surfaces. Relatively Figure 22 (d) shows that the composite 2NCO/40FO catalysts allow accessibility to the surfaces of the catalyst particles. This reasoning was supported by SEM micrographs of the catalysts. The particles were well dispersed, less agglomerated, and decreased in particle size[103].

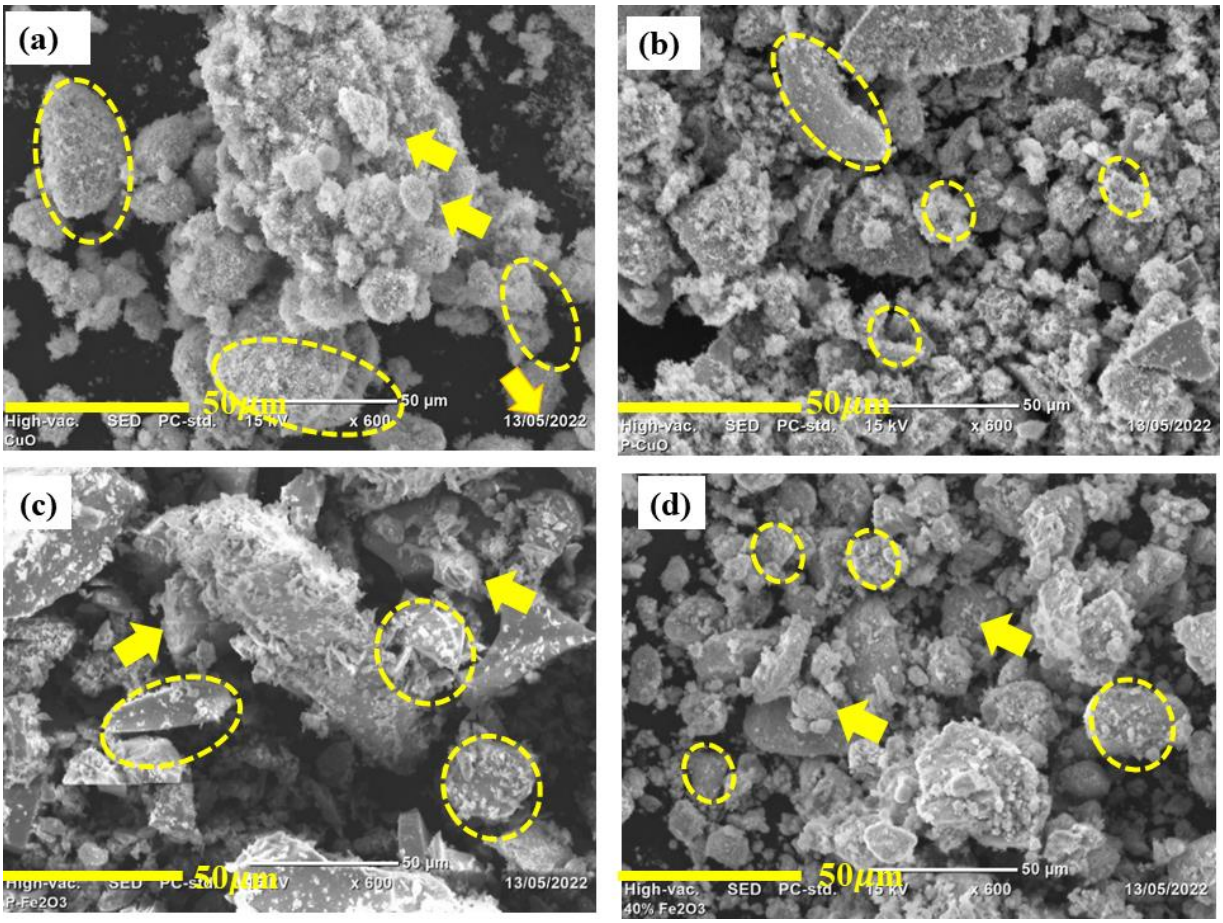

Figure 22. *SEM morphological analysis of (a) CuO, (b) p-CuO, (c) Fe2O3, and (d) 2NCO/40FO.*

4.5 BET surface area and N_2 adsorption/desorption isotherms

Based on nitrogen adsorption isotherm observations at 77 K, the Brunauer-Emmett-Teller (BET) method is typically used to compute the specific surface area. The obtained samples CuO, P-CuO, Fe_2O_3, and 2NCO/40FO BET surface areas, pore volumes, and average pore diameters are listed in Table 4. The surface area and pore volume of copper oxide made with plant extract show better surface area and pore volume than copper oxide without plant extract. The surface

area and pore volume of Fe_2O_3 and 2NCO/40FO were better than copper oxide. The blocking surface of the produced samples by associated organic compounds from the plant extract could explain the increase in specific surface area and pore volume. The result shows that CuO, *p*-CuO, Fe_2O_3, and 2NCO/40FO shows similar pore size. The greater the surface area, and pore volume the greater the number of active sites for molecule adsorption. As a result, it will eventually produce an effective photocatalysis[109].

Table 4. *Surface area, pore volume, and pore size of CuO, p-CuO, Fe_2O_3, and 2NCO/40FO.*

Name of sample	Surface area (m^2/g)	Pore Volume(cm^3/g)	Pore Size(nm)
CuO	223.667	7.272	1324
p-CuO	246.508	7.477	1324
Fe_2O_3	257.692	7.559	1324
2NCO/40FO	263.909	7.805	1324

4.6 UV- Vis, and Optical Studies

Figure 23(a) and (b) show that optical absorption spectra of the samples CuO, Fe_2O_3, 1NCO, 2NCO, 3NCO, 4NCO, 2NCO/10FO, 2NCO/20FO, 2NCO/30FO, and 2NCO/40FO, 2NCO/50FO exhibit band edge absorption peak at 367.44 nm. Figure 23(a) shows the absorbance of Fe_2O_3 was better than bare CuO. The absorbance property of bare CuO increased when doped with 1% Ni its absorbance was increased by increasing the doping concentration to 2% Ni. With the increase of Ni concentration from 3% to 4% on CuO, the absorbance property is decreased. The 2% Ni-doped CuO shows maximum absorption property due to the free-electron carrier density being high enough[93]. Figure 23(b) shows the increase in the concentration of Fe_2O_3 on 2NCO the absorption property increased in 2NCO/10FO, 2NCO/20FO, 2NCO/30FO, and 2NCO/40FO due to the synergetic effect of 2NCO and Fe_2O_3 the 2NCO/40FO shows maximum absorbance property. The absorbance of 2NCO/50FO decreased because the catalyst was not comparable to absorb.

Figure 23(c) shows that the optical band gap values estimation of samples CuO, 2NCO, Fe_2O_3, and 2NCO/40FO is 2.2, 2.17, 2.3, and 1.7 eV respectively which is calculated using the Tauc relation equation 14

$$(ahv)^2=A(hv-E_g) \quad (14)$$

'Eg' stands for optical bandgap energy, 'v' for frequency, 'h' for Planck's constant, and 'A' for a transition probability constant[110]. The bandgap value clearly shows that 2NCO/40FO reduces the bandgap energy. The catalyst absorbs more light as the bandgap narrows, allowing electrons to readily jump from the valance to the conduction band. The formation of electron and hole pairs is essential in the dye degradation process.

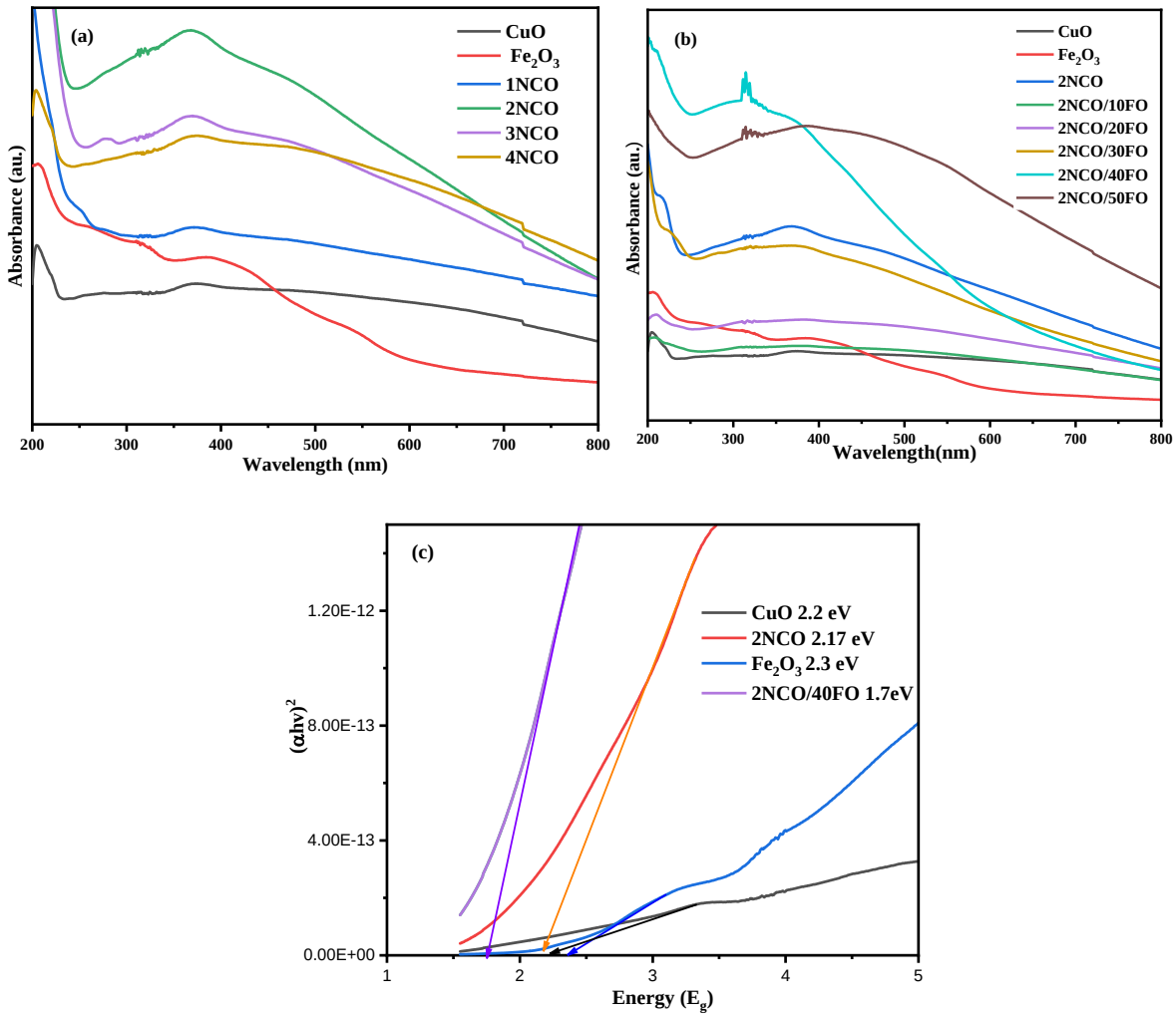

Figure 23. *Absorbance spectra of (a) CuO, Fe_2O_3, 1NCO,2NCO, 3NCO, 4NCO; (b) CuO, Fe_2O_3, 2NCO/10FO, 2NCO/20FO, 2NCO/30FO, 2NCO/40FO, and 2NCO/50FO; Tauc plot optical band gap estimation (c) CuO, 2NCO, Fe_2O_3 and 2NCO/40FO.*

4.7 Photoluminescence (PL) Analysis

PL investigations were carried out to explore the separation rate of excited electrons and holes because a rise in the recombination rate of the electron-hole pair suppresses the peak. From the comparative PL spectra presented in Figure 24, of synthesized CuO, 2NCO, Fe_2O_3, and

2NCO/40FO. The PL exhibited emission peaks in the 424.94 nm region under an excitation wavelength of 270 nm. The PL intensity of Fe_2O_3 and 2NCO was found to be lower than that of pure CuO, indicating that Fe_2O_3 and 2NCO had greater charge separation than bare CuO due to the bandgap and surface defects lattice or interstitial defects. As a result, the decrease in 2NCO/40FO PL intensity may imply a low e-/h+ pair recombination rate and high photon efficiency of the catalyst, explaining the rise in photocatalytic activity. [111].

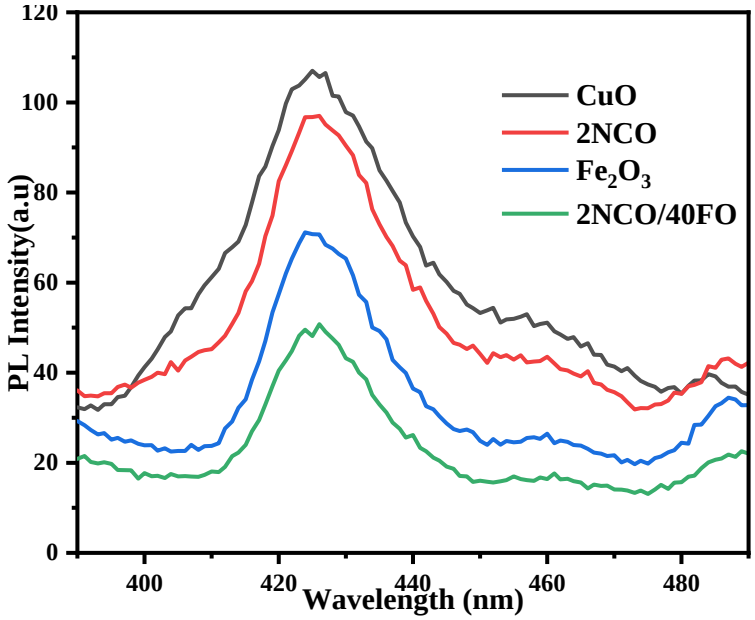

Figure 24. *PL spectra of synthesized CuO, 2NCO, Fe_2O_3, and 2NCO/40FO.*

4.8 Electrochemical impedance spectroscopy studies (EIS)

To study the charge transfer resistance electrochemical impedance analyses were used. We prepared working electrodes using the drop-casting method on the FTO glass substrate. The reference electrode was Ag/AgCl (3M KOH) electrode and a counter electrode was a platinum wire. All potentials were measured against an Ag/AgCl reference electrode using 0.5M Na_2SO_4 electrolyte as a medium. Figure 25 displays an EIS Nyquist plot to determine the property of interface charge separation. The arc radius in the EIS Nyquist plot indicates that the interface layer resistance occurs at the electrode's surface. CuO, 2NCO, Fe_2O_3, and 2NCO/40FO Nyquist plots were made between the real and imaginary impedance parts of synthesized samples, as shown below. The arc radius decreases for samples 2NCO, Fe_2O_3, and 2NCO/40FO than CuO. Due to the increased dipole moment, 2NCO/40FO has a lower arc radius than the other. The composite 2NCO/40FO allows faster charge separation and transfer of photogenerated charge

carriers during photocatalytic reaction tests. The PL result in Figure 25 confirms that composite 2NCO/40FO has better charge separation due to this the obtained composite lowers the photogenerated electron-hole pair recombination [112-114].

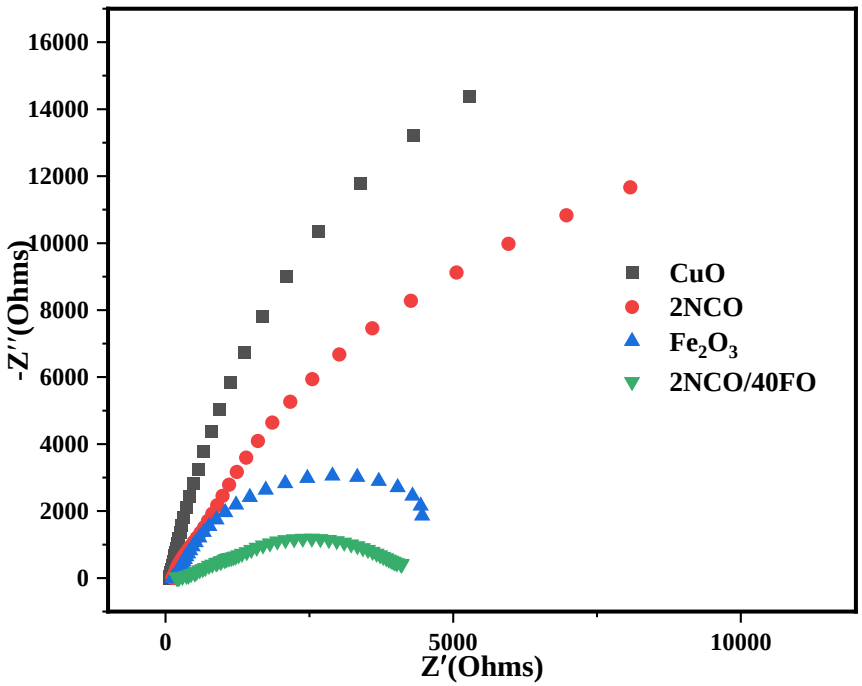

Figure 25. *EIS analysis of CuO, 2NCO, Fe_2O_3, 2NCO/40FO.*

4.9 Photocatalytic Dye Degradation

A visible light photocatalytic activity study was carried out in MB aqueous solution at room temperature using a 150 W tungsten halogen lamp light source (450 to 850 nm). UV-visible spectroscopy in the 200-800 nm range was used to examine CuO, P-CuO, Fe_2O_3, 1NCO, 2NCO, 3NCO, 4NCO, 2NCO/10FO, 2NCO/20FO, 2NCO/30FO, 2NCO/40FO, and 2NCO/50FO for discoloration. Before being irradiated, the solution was stirred for 30 min. A sample of around 6 ml was taken every 30 min up to 120 min after the light was irradiated and examined using UV-Vis Spectra spectroscopy. The degradation percentage (D%) was calculated using equation 15.

$$D\% = \frac{C_0 - C_t}{C_0} x\ 100\% \qquad (15)$$

Where, C_0 and C_t are the concentration of the dye at the irradiation for time, "0" and "t" minutes, respectively. The peak at wavelength of 664 nm decreases in intensity as the irradiation period increases. With more light exposure, the absorption peak intensity decreases rapidly. The

degradation efficiency as shown in Figure 25 calculated using equation 15 (a) CuO (68%), (b) p-CuO (74%), (c) Fe_2O_3 (84%), (d) 1NCO (76%), (e) 2NCO (81%), (f) 3NCO (78%), (g) 4NCO (77%), (h) 2NCO/10FO (81%), (i) 2NCO/20FO (84%), (j) 2NCO/30FO (86%), (k) 2NCO/40FO (94%) and (l) 2NCO/50FO (90%) at 120 min.

Due to its photogenerated charge carrier recombination, the photocatalyst efficiency of bare CuO was lower than CuO synthesized with plant extract. The plant extracted CuO was improved the surface area and charge carriers for methylene blue dye degradation [88]. in the valance band within the semiconductor. The crystalline size calculated from XRD result Doping increases the photocatalytic activity of the material by concentrating the target molecules (organic pollutants) at the catalyst surface by forming a Lewis acid-base combination. As the doping concentration is increasing the degradation efficiency is increases. The use of Ni at the donor level avoids the recombination of excited electrons and holes by Sherer's equation 11 the 2NCO showing optimum crystallinity due showing the comparable effect of the catalyst. The crystalline size was either greater than or lower than the optimum the surface area become lower so we didn't gate more active sites. As shown in Figure 23 (a) the absorbance of 2NCO has high absorption property. The material easily absorbs light and makes electrons travel from the valance band to the conduction band more than the others[115]. The 2NCO and with different loading of Fe_2O_3(10, 20, 30 ,40, and 50%) were studied. The loading of 40% Fe_2O_3 composite was degraded by 94%. The composite of 2NCO/40FO was more efficient than the bare CuO, p-CuO, 2NCO, and Fe_2O_3. This enhancement can be attributed to the fact that the composite can take advantage of a wider portion of the solar spectrum due to their different band gap value. There is synergistic effect of 2NCO and 40% Fe_2O_3 due to existence of secondary metabolites present in plant extract, and metal ions present in the composite decreased agglomeration.

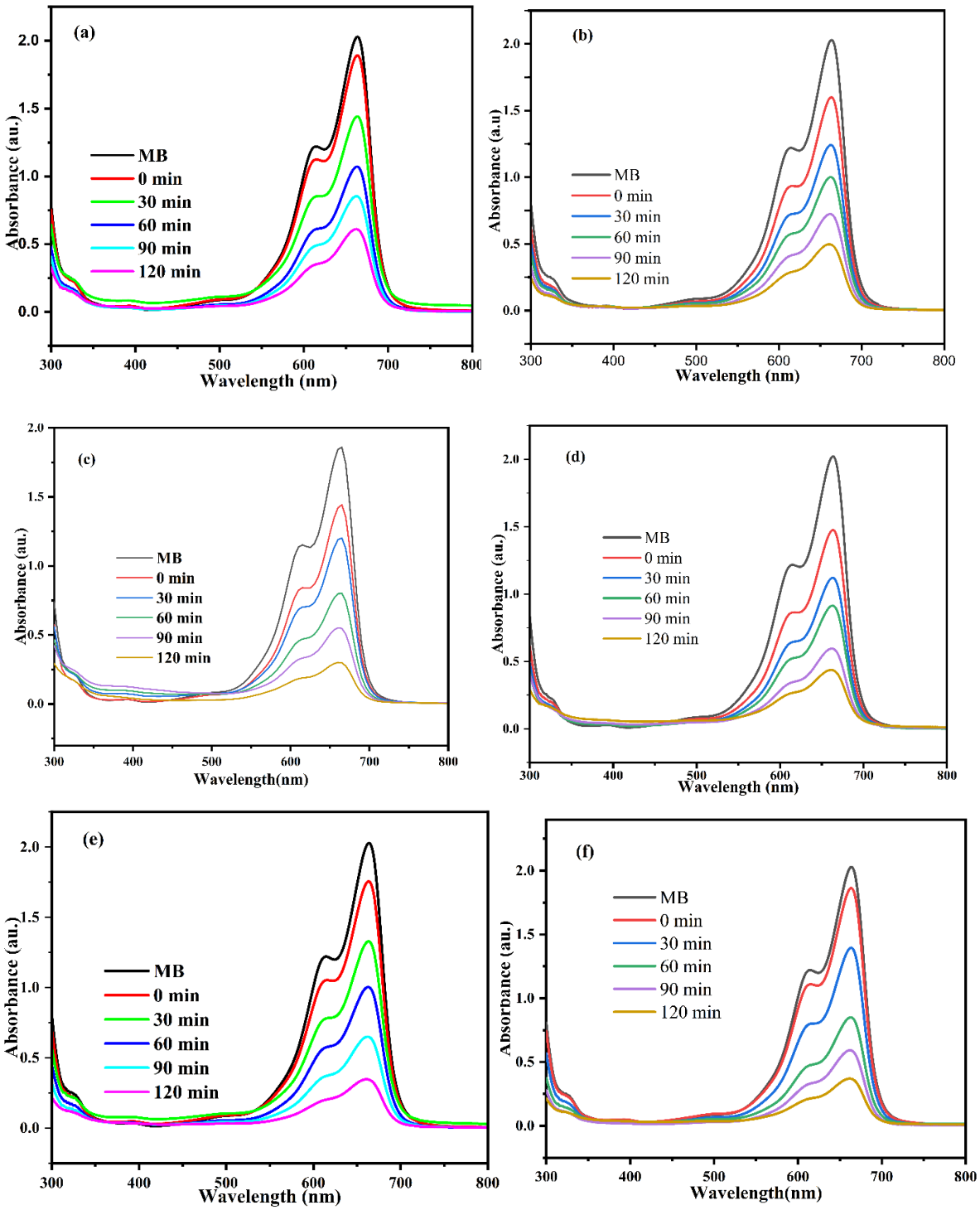
(a)
Absorbance (au.)
Wavelength (nm)
MB
0 min
30 min
60 min
90 min
120 min
(b)
Absorbance (a.u)
Wavelength (nm)
MB
0 min
30 min
60 min
90 min
120 min
(c)
Absorbance (au.)
Wavelength(nm)
MB
0 min
30 min
60 min
90 min
120 min
(d)
Absorbance (au.)
Wavelength (nm)
MB
0 min
30 min
60 min
90 min
120 min
(e)
Absorbance (au.)
Wavelength (nm)
MB
0 min
30 min
60 min
90 min
120 min
(f)
Absorbance (au.)
Wavelength(nm)
MB
0 min
30 min
60 min
90 min
120 min

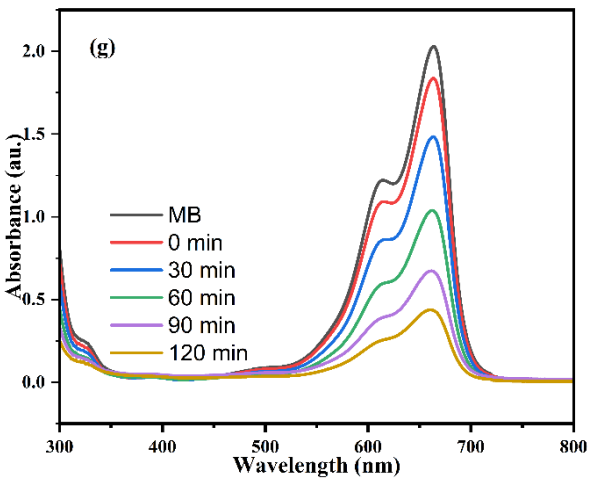
(g)
Absorbance (au.)
Wavelength (nm)
MB
0 min
30 min
60 min
90 min
120 min

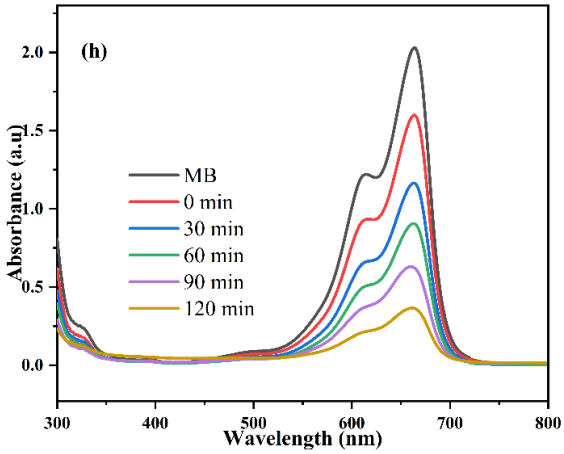
(h)
Absorbance (a.u)
Wavelength (nm)
MB
0 min
30 min
60 min
90 min
120 min

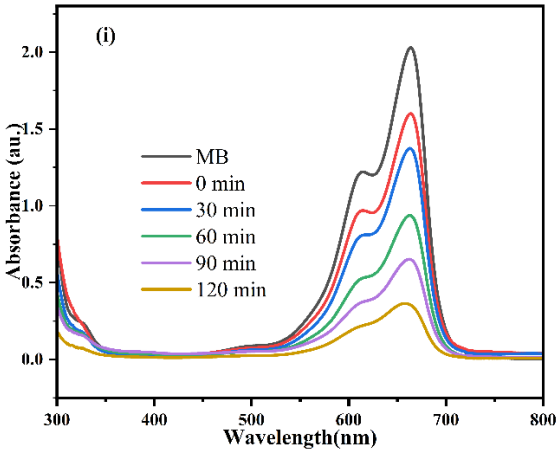
(i)
Absorbance (au.)
Wavelength(nm)
MB
0 min
30 min
60 min
90 min
120 min

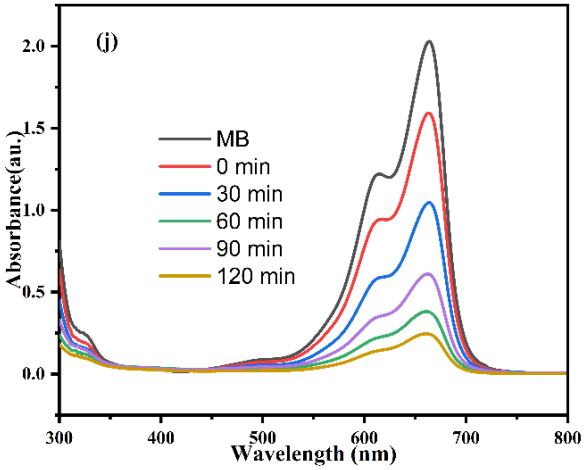
(j)
Absorbance(au.)
Wavelength (nm)
MB
0 min
30 min
60 min
90 min
120 min

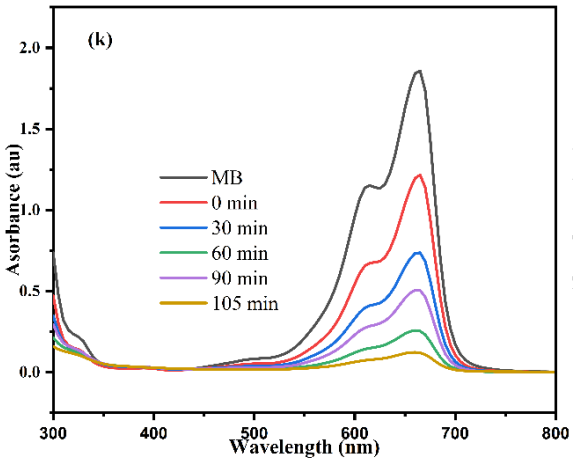
(k)
Asorbance (au)
Wavelength (nm)
MB
0 min
30 min
60 min
90 min
105 min

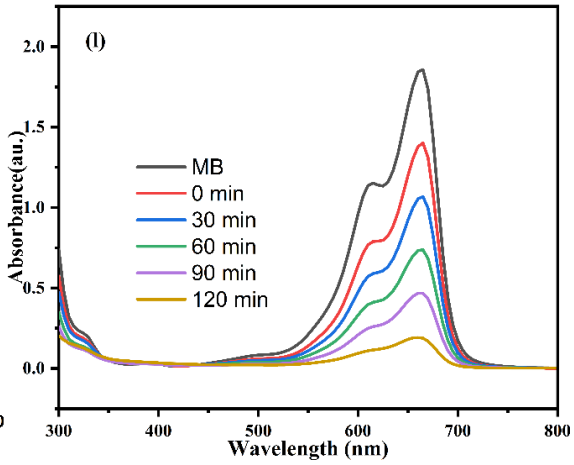
(l)
Absorbance(au.)
Wavelength (nm)
MB
0 min
30 min
60 min
90 min
120 min

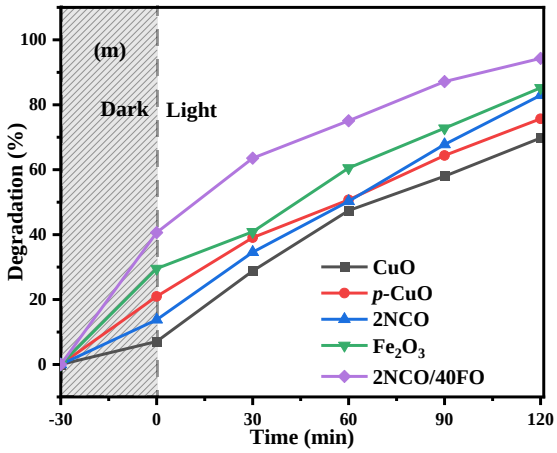

Figure 26. *UV-Vis absorption spectra of MB solution at different light exposure time durations of (a) CuO, (b) p-CuO, (c) Fe_2O_3, (d)1NCO, (e)2NCO, (f)3NCO, (g) 4NCO, (h)2NCO/10FO, (i) 2NCO/20FO, (j) 2NCO/30FO, (k) 2NCO/40FO and (l) 2NCO/50FO; the degradation performance of MB (m) CuO, p-CuO, Fe_2O_3, and 2NCO/40FO.*

4.10 Kinetics Study

The photodegradation rates of MB were faster with 2NCO/40FO composite than bare CuO under the same conditions, as shown in Figure 27 (a). The pseudo 1st order modal was used to study the kinetic degradation of MB dye photodegradation at neutral pH utilizing CuO, *p*-CuO, Fe_2O_3 2NCO, and 2NCO/40FO composite using equation 16.

$$-\ln\frac{C_t}{C_o}=kt \qquad (16)$$

Where C_t is the concentration of MB at irradiation time t, C_0 is the initial concentration before irradiation, and K is the 1st order rate constant (min^{-1})[116]. Then plotting ln (C_t/C_o) vs t as shown in Figure 27(b) and the value of reaction rate were exhibited in Figure 27(c) was calculated for CuO, *p*-CuO, 2NCO, Fe_2O_3 and 2NCO/40FO, to be 0.00969, 0.01147, 0.01322, 0.01498, 0.02301, 0.77079, 0.84899, 1.619 1.57458, 3.35464 min^{-1}, respectively. 2NCO/40FO shows a higher kinetic rate than pure CuO and the introduction of Fe_2O_3 in 2NCO can further increase to some extent. The data fitted well and gave a correlation coefficient of CuO, *p*-CuO, 2NCO, Fe_2O_3, and 2NCO/40FO to be 0.95705, 0.93844, 0.94696, 0.93711,0.93389, at the neutral pH respectively.

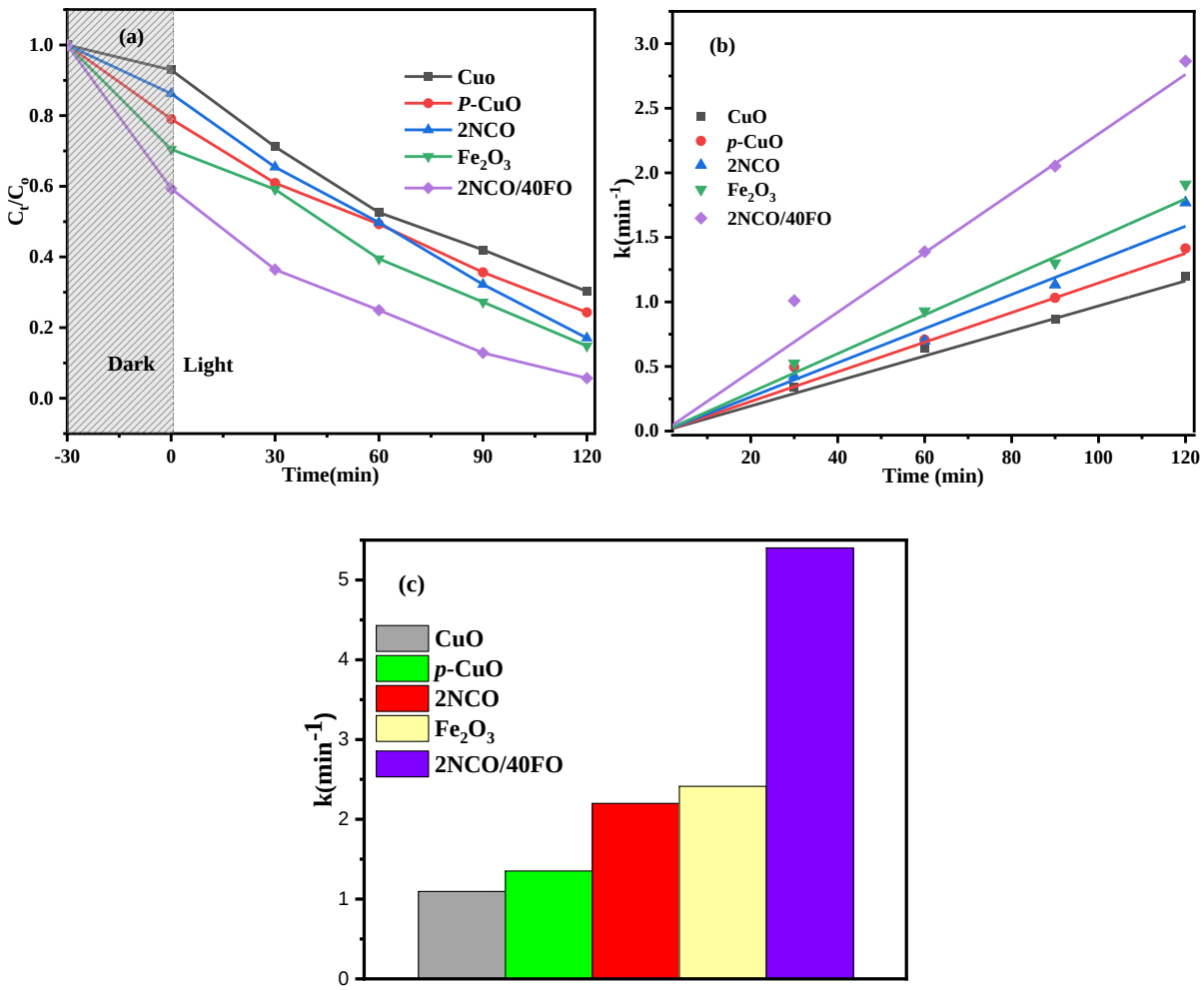

Figure 27. *(a)The variation of MB concentration under visible irradiation at different periods, (b) the consistent reaction kinetics of photodegradation of MB, (c) the reaction rate constant of CuO, p-CuO, 2NCO, Fe_2O_3, and 2NCO/40FO catalysts.*

4.11 Stability and Recyclability

For pilot-scale remediation systems, recovery and reusability are critical parameters to consider when choosing a cost-effective and viable catalyst. Using 0.125 g catalyst in 500 ml of the MB dye, the reusability of our best composite was studied for five cycles of MB photo-degradation. Figure 28 shows the 2NCO/40FO catalyst's recyclability and stability after five cycles during the 120 min reaction. After the treatment, the catalyst may be easily recycled and reused. With successive high-efficiency cycles, the performance of 2NCO/40FO fell from 94 to 80% after five cycles. The following reasons could have played a role in the decrease in photocatalysis activity: (1) There may be material losses during the recovery process (washing and drying), resulting in a reduced dose in subsequent cycles, lowering surface catalytic activity and lowering

performance[117]. (2)During the five cycles the reduction in the effective surface area reduces the number of active sites and fouling may alter[118]. The recyclability and stability test showed the catalyst was stable up to five cycles and the XRD result of reused catalyst showed the reused material show no change in the XRD pattern. According to the findings, current materials systems can degrade an organic MB dye derived from industrial effluents produced by diverse processing companies. As a result, the 2NCO/40FO photocatalyst was no significant change for up to five cycles for degrading of MB.

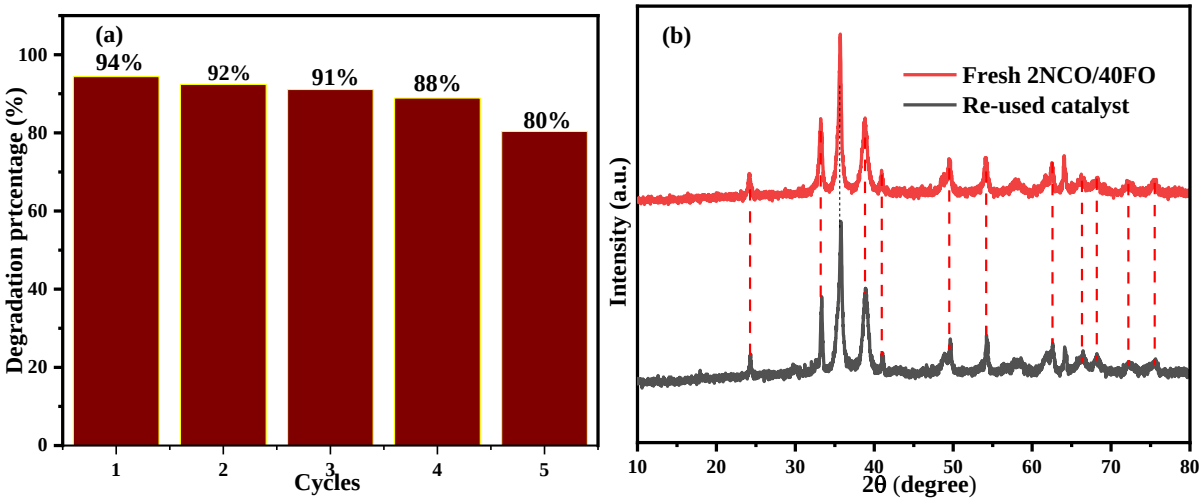

Figure 28. *(a) Bar graph of Stability and Recyclability; (b) XRD pattern of fresh 2NCO/40FO and re-used catalyst.*

4.12 Dye Degradation Mechanism of 2NCO/40FO Composite

Both CuO and Fe_2O_3 valence band (VB) electrons are promoted to the conductive band (CB) during UV light irradiation, leaving holes in the VB (h^+ VB). The photocatalytic mechanism of CuO/Fe_2O_3 composites were depicted in Figure 29. The heterostructure creates a good couple, which helps separate the created electron-hole pairs[119]. CuO was doped with nickel (2%) to improve its electron transport properties. Due to the difference in conduction band levels, electrons stored in the CuO conduction band travel to the Fe_2O_3 conduction band. Furthermore, the reaction between absorbed oxygen (O_2) and the electron collected at the surface of Fe_2O_3 results in the formation of superoxide radical ($\bullet O_2^-$) as the electrons in the conduction band of Fe_2O_3 reduce absorbed O_2. The MB dye was degraded by the superoxide radical and electrons that were generated[120]. However, the holes in CuO's and Fe_2O_3 of the valence band barely met the criteria for the formation of hydroxyl radicals (•OH) generation ($H_2O/•OH^-$) instead

(•OH) formed from the intermediate reaction shown in the equation. As shown in the equations below, the holes and hydroxyl radicals may play a role in the degradation process. Finally, the process produced intermediate molecules such as H_2O and CO_2.

$$CuO\ (e^-+h^+)/Fe_2O_3(e^-+h^+) \rightarrow CuO\ (e^-+h^+)\ Fe_2O_3 \quad (17)$$

$$h^+ + OH^- \rightarrow OH \quad (18)$$

$$e^- + O_2 \rightarrow \bullet O^-_2 \quad (19)$$

$$H_2O + \bullet O^-_2 \rightarrow \bullet OOH + OH \quad (20)$$

$$2OOH\bullet + O_2 \rightarrow H_2O_2 \quad (21)$$

$$H_2O_2 + \bullet O^-_2 \rightarrow \bullet OH + OH^- + O_2 \quad (22)$$

$$\bullet OH + \bullet O^-_2 + hv + \text{pollutant} \rightarrow \text{degrade pollutant} \quad (23)$$

$$\bullet OH + \bullet O^-_2 + hv + \text{degrade pollutant} \rightarrow CO_2 + H_2O \quad (24)$$

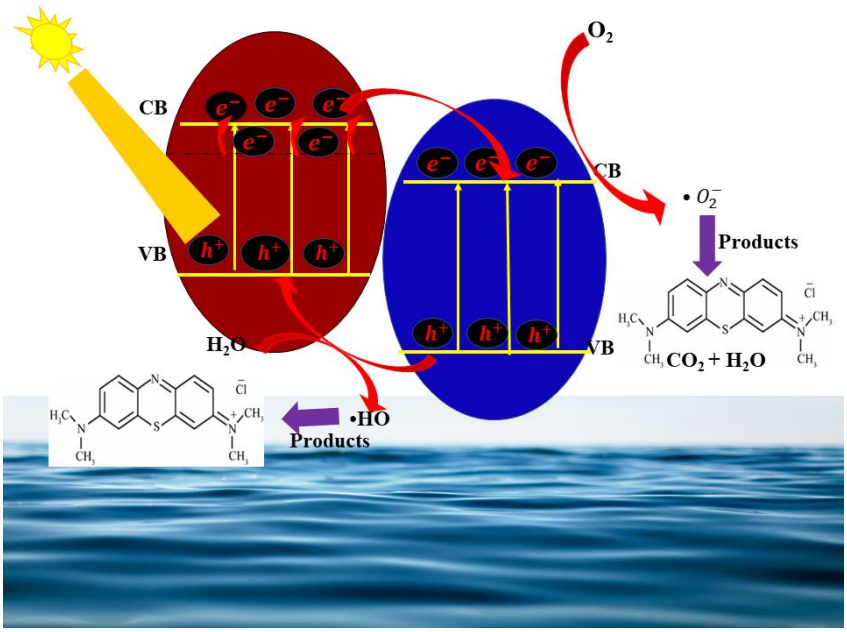

Figure 29. *Mechanism of photodegradation of 2NCO/40FO.*

5. CONCLUSION AND RECOMMENDATION

5.1 Conclusion

In the present work, CuO, *p*-CuO, Fe_2O_3, 1NCO, 2NCO, 3NCO, 4NCO, 2NCO/10FO, 2NCO/20FO, 2NCO/30FO, 2NCO/40FO, and 2NCO/50FO catalyst were successfully synthesized by green synthesis method. XRD, TGA, FTIR, PL and EIS. The 2NCO/40FO lowered the recombination and better charge transfer resistance. The performance of Bare CuO was 68% the biosynthesized CuO shows better degradation performance and the synthesized Fe_2O_3 showed a degradation percentage of 81%. Optimization of Ni-doped copper oxide with a doping concentration of 1, 2, 3, and 4% was investigated from absorbance and performance value. The 2% Ni-doped copper oxide was 80% maximum absorbance properties of doped samples. The enhanced photocatalytic property was evaluated by coupling 2NCO coupled with Fe_2O_3 with weight percentages of 10, 20, 30, 40, and 50%. The composite of 2NCO/40FO was shown 94% and better absorbance properties. The recyclability and stability test showed the catalyst was stable up to 5 cycles and the XRD result of reused catalyst showed the reused material show no change in the XRD pattern. According to the findings, current materials systems can degrade an organic MB dye derived from industrial effluents produced by diverse processing companies.

5.2 Recommendation

We suggest, X-ray photoelectron spectroscopy (XPS) for surface chemical analysis, to determine the elemental composition, empirical formula, chemical state, and electronic state of the elements present in a material. It is difficult to know the oxidation state of Ni^{2+} or Ni^{3+} many findings show that the oxidation state of Ni is 2+ but it is difficult to be sure of being 2+ without characterization of XPS. Scanning electron microscopy (SEM) helps to visualize and further design the surface morphologies and particle size of the composite powder. They allow a better understanding of surface morphology. It is difficult to explain the surface property with this magnification.

REFERENCES

1. Salehi, M. (2022) *Global water shortage and potable water safety; Today's concern and tomorrow's crisis.* Environment International,. 158: p. 106936.
2. Tariq, H., et al. (2022), *Mechanical Performance of Polymeric ARGF-Based Fly Ash-Concrete Composites: A Study for Eco-Friendly Circular Economy Application.* Polymers,. 14(9): p. 1774.
3. Nasrollahi, N., V. Vatanpour, and A. Khataee (2022), *Removal of antibiotics from wastewaters by membrane technology: Limitations, successes, and future improvements.* Science of The Total Environment,: p. 156010.
4. Artioli, Y. (2008), *Adsorption*, in *Encyclopedia of Ecology*, S.E. Jørgensen and B.D. Fath, Editors., Academic Press: Oxford. p. 60-65.
5. Crawford, R.L. (2011), *6.02 - Biodegradation: Principles, Scope, and Technologies*, in *Comprehensive Biotechnology (Second Edition)*, M. Moo-Young, Editor., Academic Press: Burlington. p. 3-13.
6. Rodriguez-Narvaez, O.M., et al. (2017), *Treatment technologies for emerging contaminants in water: A review.* Chemical Engineering Journal,. 323: p. 361-380.
7. Jalali, S., et al. (2019), *One step integration of plasmonic Ag_2CrO_4/Ag/AgCl into HKUST-1-MOF as novel visible-light driven photocatalyst for highly efficient degradation of mixture dyes pollutants: Its photocatalytic mechanism and modeling.* Polyhedron,. 166: p. 217-225.
8. Sivaraman, C., et al.(2022), *Current Developments in the Effective Removal of Environmental Pollutants through Photocatalytic Degradation Using Nanomaterials.* Catalysts,. 12(5): p. 544.
9. Kiwaan, H.A., et al. (2020), *Photocatalytic degradation of organic dyes in the presence of nanostructured titanium dioxide.* Journal of Molecular Structure,. 1200: p. 127115.
10. Salama, A., et al. (2018), *Photocatalytic degradation of organic dyes using composite nanofibers under UV irradiation.* Applied Nanoscience,. 8(1): p. 155-161.
11. Sacco, O., et al., *Photocatalytic Degradation of Organic Dyes under Visible Light on N-Doped <svg style="vertical-align:-4.32007pt;width:42.637501px;" id="M1" height="20.637501" version="1.1" viewBox="0 0 42.637501 20.637501" width="42.637501" xmlns:xlink="http://www.w3.org/1999/xlink"*
12. Stylidi, M. (2003), D.I. Kondarides, and X.E. Verykios, *Pathways of solar light-induced photocatalytic degradation of azo dyes in aqueous TiO_2 suspensions.* Applied Catalysis B: Environmental,. 40(4): p. 271-286.
13. Kahsay, M.H., et al., *Green synthesis of zinc oxide nanostructures and investigation of their photocatalytic and bactericidal applications.* RSC Advances, 2019. 9(63): p. 36967-36981.
14. Liu, H., et al. (2007), *Catalytic synthesis of nanosized hematite particles in solution.* Materials Chemistry and Physics,. 102(1): p. 1-6.
15. Song, K., et al., (2011), *A wireless electronic nose system using a Fe_2O_3 gas sensing array and least squares support vector regression.* Sensors,. 11(1): p. 485-505.
16. Bomio, M., P. Lavela, and J. Tirado (2008). *Electrochemical evaluation of CuFe2O4 samples obtained by sol–gel methods used as anodes in lithium batteries.* Journal of Solid State Electrochemistry, 12(6): p. 729-737.

17. Wang, Y., et al. (2010), *Catalytic activity of nanometer-sized CuO/Fe2O3 on thermal decompositon of AP and combustion of AP-based propellant.* Combustion Science and Technology,. 183(2): p. 154-162.
18. Liu, X.-M., et al. (2009), *Fabrication of CuO/Fe2O3 hollow hybrid microspheres.* Materials Chemistry and Physics,. 113(2-3): p. 518-522.
19. Li, Y. and Y.-L. Wu et al. (2003), *An over four millennium story behind qinghaosu (artemisinin)-a fantastic antimalarial drug from a traditional Chinese herb.* Current medicinal chemistry,. 10(21): p. 2197-2230.
20. Ma, X., et al. (2011), *Preparation, characterization and catalytic behavior of hierachically porous CuO/α-Fe_2O_3/SiO_2 composite material for CO and o-DCB oxidation.* Journal of natural gas chemistry,. 20(6): p. 618-622.
21. Nair, G.B., V.B. Pawade, and S.J. Dhoble et al, (2018), *White light-emitting novel nanophosphors for LED applications*, in *Nanomaterials for Green Energy*., Elsevier. p. 411-431.
22. Gao, W., et al. (2010), *Synthesis and magnetic properties of Mn doped CuO nanowires.* Physics Letters A,. 375(2): p. 180-182.
23. Meneses, C., et al. (2008), *Synthesis and characterization of TM-doped CuO (TM= Fe, Ni).* Journal of non-crystalline solids,. 354(42-44): p. 4830-4832.
24. Gülen, Y., et al. (2013), *Fabrication and characterization of Mn-doped CuO thin films by the SILAR method.* Ceramics International,. 39(6): p. 6475-6480.
25. López-Pacheco, I.Y., et al. (2019), *Anthropogenic contaminants of high concern: existence in water resources and their adverse effects.* Science of the Total environment,. 690: p. 1068-1088.
26. Sorome, D. (2020), *Synthesis, characterizations and performance evaluation of Ag/Ag_2O/$ZnFe_2O_4$ composite materials for organic dye degradation*., ASTU.
27. Alimuddin, A.H., et al. (2011), *SYNTHESIS OF 5, 7-DIHYDROXY-3', 4'-DIMETHOXYISOFLAVON FROM EUGENOL.* Indonesian Journal of Chemistry,. 11(3): p. 229-233.
28. Naik, M.M., et al. (2019), *Green synthesis of zinc doped cobalt ferrite nanoparticles: Structural, optical, photocatalytic and antibacterial studies.* Nano-Structures & Nano-Objects,. 19: p. 100322.
29. Zhao, Y., et al. (2009), *Adsorption of Hg^{2+} from aqueous solution onto polyacrylamide/attapulgite.* Journal of Hazardous Materials,. 171(1-3): p. 640-646.
30. Kaur, K. et al. (2018), *Synergistic effect of organic-inorganic hybrid nanocomposite ion exchanger on photocatalytic degradation of Rhodamine-B dye and heavy metal ion removal from industrial effluents.* Journal of Environmental Chemical Engineering,. 6(6): p. 7091-7101.
31. Xie, Y. et al. (2006) *Interactive oxidation of photoelectrocatalysis and electro-Fenton for azo dye degradation using TiO_2–Ti mesh and reticulated vitreous carbon electrodes.* Materials Chemistry and Physics,. 95(1): p. 39-50.
32. Zhao, C., et al. (2022), *Synthesis of Two-Dimensional Ultrathin Photocatalytic Materials toward more Sustainable Environment.* Green Chemistry,.
33. Smit, A.T., et al. (2022), *Biomass Pre-Extraction as a Versatile Strategy to Improve Biorefinery Feedstock Flexibility, Sugar Yields, and Lignin Purity.* ACS sustainable chemistry & engineering.

34. Baskar, A.V., et al. (2022), *Recovery, regeneration and sustainable management of spent adsorbents from wastewater treatment streams: A review.* Science of The Total Environment,: p. 153555.
35. Lauesen, L.M. (2022), *Advanced wastewater treatment of micropollutants–state of the art.* Technological Sustainability,.
36. Zhang, M.-h., et al. (2019), *A review on Fenton process for organic wastewater treatment based on optimization perspective.* Science of the Total Environment,. 670: p. 110-121.
37. Martínez-Sánchez, C., E.B. Bustos, and A. Sandoval-González (2022), *Influence of Nanomaterials in Combined Microbial Fuel Cell-Electro-Fenton Systems as a Sustainable Alternative for Electricity Generation and Wastewater Treatment*, in *Innovations in Environmental Biotechnology*. Springer. p. 677-704.
38. Fronzi, M. et al. (2017), *Surface modification of perfect and hydroxylated TiO2 rutile (110) and anatase (101) with chromium oxide nanoclusters.* ACS omega,. 2(10): p. 6795-6808.
39. Korotcov, A.V., et al. (2007), *Raman scattering characterization of well-aligned RuO2 and IrO2 nanocrystals.* Journal of Raman Spectroscopy: An International Journal for Original Work in all Aspects of Raman Spectroscopy, Including Higher Order Processes, and also Brillouin and Rayleigh Scattering,. 38(6): p. 737-749.
40. Ziaja, B., et al. (2015), *Time-resolved observation of band-gap shrinking and electron-lattice thermalization within X-ray excited gallium arsenide.* Scientific reports,. 5(1): p. 1-7.
41. Samanta, B., et al. (2022), *Challenges of modeling nanostructured materials for photocatalytic water splitting.* Chemical Society Reviews,.
42. Singh, A. and B.K. Mishra (2022), *Treatment aspect of an emerging pollutant from Pharmaceutical industries using advanced oxidation process: past, current, and future trends*, in *Development in Wastewater Treatment Research and Processes*. Elsevier. p. 23-44.
43. Liu, Z., et al. (2007), *An efficient bicomponent TiO_2/SnO_2 nanofiber photocatalyst fabricated by electrospinning with a side-by-side dual spinneret method.* Nano letters,. 7(4): p. 1081-1085.
44. Linsebigler, A.L., G. Lu, and J.T. Yates Jr, *Photocatalysis on TiO_2 surfaces: principles, mechanisms, and selected results.* Chemical reviews, 1995. 95(3): p. 735-758.
45. Li, T., et al. (2022), *$NiCo_2O_4/BiOCl/Bi_2O_3Br$ ternary Z-scheme heterojunction enhance peroxymonosulfate activation under visible light: Catalyst synthesis and reaction mechanism.* Chinese Chemical Letters,.
46. Zhang, X., et al. (2022), *In-situ synthesis of dual Z-scheme heterojunctions of cuprous oxide/layered double hydroxides/nitrogen-rich graphitic carbon nitride for photocatalytic sterilization.* Journal of Colloid and Interface Science,. 620: p. 313-321.
47. Sakthivel, C.et al.(2022) *Comparison of the effectiveness of melamine derived graphitic carbon nitrides based photocatalysts towards the degradation of Rhodamine B.* Materials Today: Proceedings,.
48. Li, J. et al. (2015) *Semiconductor-based photocatalysts and photoelectrochemical cells for solar fuel generation: a review.* Catalysis Science & Technology,. 5(3): p. 1360-1384.

49. Pehkonen, S., et al. (1993), *Photocatalystic Oxidation of Organic Acids on Quantum-Sized Semiconductor Colloids.* Environ. Sci. Technol,. 26: p. 2056.
50. K. Pillay, (2019) *Synthesis of N-doped ZnO nanoparticles with cabbage morphology as a catalyst for the efficient photocatalytic degradation of methylene blue under UV and visible light.* RSC Advances,. 9(13): p. 7509-7535.
51. Lamba, R., et al. (2017), *Enhanced visible light driven photocatalytic application of Ag_2O decorated ZnO nanorods heterostructures.* Separation and Purification Technology,. 183: p. 341-349.
52. Lenin, N., et al., *Electrical and magnetic behavior of iron doped nickel titanate ($Fe^{3+}/NiTiO_3$) magnetic nanoparticles.* Journal of Magnetism and Magnetic Materials, 2016. 397: p. 281-286.
53. Dai, Z., et al. (2016), *Crystal defect engineering of aurivillius Bi_2MoO_6 by Ce doping for increased reactive species production in photocatalysis.* ACS Catalysis,. 6(5): p. 3180-3192.
54. Raizada, P., et al. (2019), *Ag_3PO_4 modified phosphorus and sulphur co-doped graphitic carbon nitride as a direct Z-scheme photocatalyst for 2, 4-dimethyl phenol degradation.* Journal of Photochemistry and Photobiology A: Chemistry,. 374: p. 22-35.
55. Anandan, S. et al. (2007) *Emergent methods to synthesize and characterize semiconductor CuO nanoparticles with various morphologies – an overview.* Journal of Experimental Nanoscience,. 2(1-2): p. 23-56.
56. Narayanan, R. and M.A. El-Sayed, *Catalysis with Transition Metal Nanoparticles in Colloidal Solution: Nanoparticle Shape Dependence and Stability.* The Journal of Physical Chemistry B, 2005. 109(26): p. 12663-12676.
57. Kumar, S.G. and K.K. Rao, *Tungsten-based nanomaterials (WO3 & Bi2WO6): modifications related to charge carrier transfer mechanisms and photocatalytic applications.* Applied Surface Science, 2015. 355: p. 939-958.
58. Kumar, S., et al., *Curcumin functionalized CuO/Ag nanocomposite: Efficient visible light Z-scheme photocatalyst for methyl orange degradation.* Environmental Nanotechnology, Monitoring & Management, 2019. 12: p. 100236.
59. Chang, Y.-C. and J.-Y. Guo, *Double-sided plasmonic silver nanoparticles decorated copper oxide/zinc oxide heterostructured nanomaces with improving photocatalytic performance.* Journal of Photochemistry and Photobiology A: Chemistry, 2019. 378: p. 184-191.
60. Liu, Y., et al., *Anion-controlled construction of CuO honeycombs and flowerlike assemblies on copper foils.* Crystal growth & design, 2007. 7(3): p. 467-470.
61. Ray, S.C., *Preparation of copper oxide thin film by the sol–gel-like dip technique and study of their structural and optical properties.* Solar Energy Materials and Solar Cells, 2001. 68(3): p. 307-312.
62. Kum, J.M., et al., *Photocatalytic hydrogen production over CuO and TiO2 nanoparticles mixture.* International Journal of Hydrogen Energy, 2013. 38(31): p. 13541-13546.
63. Gao, W., et al., *Molecular description of copper (I) oxide and copper (II) oxide.* Quimica Nova, 2018. 41: p. 874-879.
64. Priya, B., et al., *Photocatalytic mineralization and degradation kinetics of ampicillin and oxytetracycline antibiotics using graphene sand composite and chitosan supported BiOCl.* Journal of Molecular Catalysis A: Chemical, 2016. 423: p. 400-413.

65. Raizada, P., A. Sudhaik, and P. Singh, *Photocatalytic water decontamination using graphene and ZnO coupled photocatalysts: A review.* Materials Science for Energy Technologies, 2019. 2(3): p. 509-525.
66. Xu, Q., et al., *S-scheme heterojunction photocatalyst.* Chem, 2020. 6(7): p. 1543-1559.
67. Abbas, A.M., et al. *Photocatalytic activity of Ag-ZnO nanocomposites integrated essential ginger oil fabricated by green synthesis method*. in *Journal of Physics: Conference Series*. 2021. IOP Publishing.
68. Li, Z., et al., *Applying facilely synthesized CuO/CeO2 photocatalyst to accelerate methylene blue degradation in hypersaline wastewater.* Surface and Interface Analysis, 2019. 51(3): p. 336-344.
69. Nogueira, A.C., et al., *Improved visible light photoactivity of CuBi2O4/CuO heterojunctions for photodegradation of methylene blue and metronidazole.* The Journal of Physical Chemistry C, 2019. 123(42): p. 25680-25690.
70. Batista, A.P.L., et al., *Preparation of CuO/SiO2 and photocatalytic activity by degradation of methylene blue.* Environmental Chemistry Letters, 2010. 8(1): p. 63-67.
71. Harish, S., et al., *Controlled structural and compositional characteristic of visible light active ZnO/CuO photocatalyst for the degradation of organic pollutant.* Applied Surface Science, 2017. 418: p. 103-112.
72. Virkutyte, J. and R.S. Varma, *Green synthesis of metal nanoparticles: biodegradable polymers and enzymes in stabilization and surface functionalization.* Chemical Science, 2011. 2(5): p. 837-846.
73. Raveendran, P., J. Fu, and S.L. Wallen, *Completely "green" synthesis and stabilization of metal nanoparticles.* Journal of the American Chemical Society, 2003. 125(46): p. 13940-13941.
74. Alghuthaymi, M.A., et al., *Trichoderma: An Eco-Friendly Source of Nanomaterials for Sustainable Agroecosystems.* Journal of Fungi, 2022. 8(4): p. 367.
75. Rajendaran, K., R. Muthuramalingam, and S. Ayyadurai, *Green synthesis of Ag-Mo/CuO nanoparticles using Azadirachta indica leaf extracts to study its solar photocatalytic and antimicrobial activities.* Materials Science in Semiconductor Processing, 2019. 91: p. 230-238.
76. Narayanan, K.B. and S.S. Han, *One-pot green synthesis of Hematite (α-Fe2O3) nanoparticles by ultrasonic irradiation and their in vitro cytotoxicity on human keratinocytes CRL-2310.* Journal of Cluster Science, 2016. 27(5): p. 1763-1775.
77. Archana, V., J. Joseph Prince, and S. Kalainathan, *Simple One-Step Leaf Extract-Assisted Preparation of α-Fe₂O₃ Nanoparticles, Physicochemical Properties, and Its Sunlight-Driven Photocatalytic Activity on Methylene Blue Dye Degradation.* Journal of Nanomaterials, 2021. 2021: p. 8570351.
78. Rufus, A., S. N, and D. Philip, *Synthesis of biogenic hematite (α-Fe2O3) nanoparticles for antibacterial and nanofluid applications.* RSC Advances, 2016. 6(96): p. 94206-94217.
79. Ley, J., et al., *Isolation and synthesis of acmellonate, a new unsaturated long chain 2-ketol ester from Spilanthes acmella.* Natural Product Research, 2006. 20(9): p. 798-804.
80. Rivera, V.L., *Estudos fitogeográficos em Vernonia Schreb. sensu lato (Asteraceae) no bioma Cerrado.* 2006.

81. Bandonienė, D. and M. Murkovic, *On-line HPLC-DPPH screening method for evaluation of radical scavenging phenols extracted from apples (Malus domestica L.).* Journal of Agricultural and Food Chemistry, 2002. 50(9): p. 2482-2487.
82. Neacsu, M., et al., *Phytochemical profile of commercially available food plant powders: their potential role in healthier food reformulations.* Food chemistry, 2015. 179: p. 159-169.
83. D Archivio, M., et al., *Polyphenols, dietary sources and bioavailability.* Annali-Istituto Superiore di Sanita, 2007. 43(4): p. 348.
84. S, S., et al., *Hydrothermal synthesis of novel Zn doped CuO nanoflowers as an efficient photodegradation material for textile dyes.* Materials Letters, 2015. 144: p. 127.
85. Aminuzzaman, M., L.M. Kei, and W.H. Liang. *Green synthesis of copper oxide (CuO) nanoparticles using banana peel extract and their photocatalytic activities*. in *AIP Conference Proceedings*. 2017. AIP Publishing LLC.
86. Bhattacharjee, A. and M. Ahmaruzzaman, *Microwave assisted facile and green route for synthesis of CuO nanoleaves and their efficacy as a catalyst for reduction and degradation of hazardous organic compounds.* Journal of Photochemistry and Photobiology A: Chemistry, 2018. 353: p. 215-228.
87. Dulta, K., et al., *Multifunctional CuO nanoparticles with enhanced photocatalytic dye degradation and antibacterial activity.* Sustainable Environment Research, 2022. 32(1): p. 2.
88. Parvathiraja, C. and S. Shailajha, *Bioproduction of CuO and Ag/CuO heterogeneous photocatalysis-photocatalytic dye degradation and biological activities.* Applied Nanoscience, 2021. 11(4): p. 1411-1425.
89. Siddiqui, H., M.S. Qureshi, and F.Z. Haque, *Biosynthesis of Flower-Shaped CuO Nanostructures and Their Photocatalytic and Antibacterial Activities.* Nano-Micro Letters, 2020. 12(1): p. 29.
90. Kumari, V., S. Kaushal, and P.P. Singh, *Green synthesis of a CuO/rGO nanocomposite using a Terminalia arjuna bark extract and its catalytic activity for the purification of water.* Materials Advances, 2022. 3(4): p. 2170-2184.
91. Ren, B., et al., *A grape-like N-doped carbon/CuO-Fe2O3 nanocomposite as a highly active heterogeneous Fenton-like catalyst in methylene blue degradation.* Journal of Cleaner Production, 2019. 240: p. 118143.
92. Sun, M., et al., *Mg doped CuO–Fe2O3 composites activated by persulfate as highly active heterogeneous catalysts for the degradation of organic pollutants.* Journal of Alloys and Compounds, 2020. 825: p. 154036.
93. George, A., et al. (2022), *Photocatalytic effect of CuO nanoparticles flower-like 3D nanostructures under visible light irradiation with the degradation of methylene blue (MB) dye for environmental application.* Environmental Research,. 203: p. 111880.
94. Kang, Y.S., et al., *Synthesis and characterization of nanometer-size Fe_3O_4 and γ-Fe_2O_3 particles.* Chemistry of Materials, 1996. 8(9): p. 2209-2211.
95. Parvathiraja, C., et al. (2021), *Biosynthesis of silver nanoparticles by Cyperus pangorei and its potential in structural, optical and catalytic dye degradation.* Applied Nanoscience,. 11(2): p. 477-491.
96. Raizada, P., et al. (2020), *Engineering nanostructures of CuO-based photocatalysts for water treatment: current progress and future challenges.* Arabian Journal of Chemistry,. 13(11): p. 8424-8457.

97. Mahadik, M., et al. (2013), *Photoelectrocatalytic oxidation of Rhodamine B with sprayed α-Fe_2O_3 photocatalyst.* Materials express,. 3(3): p. 247-255.
98. V. Rajendran, (2017) *Synthesis and characterization of CuS nanostructures: structural, optical, electrochemical and photocatalytic activity by the hydro/solvothermal process.* International Journal of Hydrogen Energy,. 42(42): p. 26454-26463.
99. Devi, L.V., et al. (2017), *Effect of La doping on the lattice defects and photoluminescence properties of CuO.* Journal of Alloys and Compounds,. 709: p. 496-504.
100. Begum, et al. (2020) S., A. Esakkiraja, and S. Asan, *green synthesis, characterization and antibacterial activity of copper oxide nanoparticles synthesized using catharanthus roseus leaf extract.*.
101. Zhou, X., et al. (2016), *CuO-Fe_2O_3-CeO_2/HZSM-5 bifunctional catalyst hydrogenated CO2 for enhanced dimethyl ether synthesis.* Chemical Engineering Science. 153: p. 10-20.
102. Liu, R.-w., et al.(2013), *Synthesis of Dimethyl Ether from CO2 and H2 Using a Cu–Fe–Zr/HZSM-5 Catalyst System.* Industrial & Engineering Chemistry Research,. 52(47): p. 16648-16655.
103. Bonura, G., et al. (2014), *Catalytic behaviour of a bifunctional system for the one step synthesis of DME by CO_2 hydrogenation.* Catalysis today,. 228: p. 51-57.
104. Bharath, G., et al., *Solvent-free mechanochemical synthesis of graphene oxide and Fe_3O_4–reduced graphene oxide nanocomposites for sensitive detection of nitrite.* Journal of Materials Chemistry A, 2015. 3(30): p. 15529-15539.
105. Chernyshova, I., M. Hochella Jr, and A. Madden, *Size-dependent structural transformations of hematite nanoparticles. 1. Phase transition.* Physical Chemistry Chemical Physics, 2007. 9(14): p. 1736-1750.
106. Ratnawulan, R., et al. (2021), *Synthesis and Characterization of Polystyrene/CuO-Fe2O3 Nanocomposites from Natural Materials as Hydrophobic Photocatalytic Coatings.* Crystals,. 11(1): p. 31.
107. Wang, Y.,et al.(1998) *FTIR analysis of well-defined α-Fe_2O_3 particles.* Colloids and Surfaces A: Physicochemical and Engineering Aspects,. 134(3): p. 281-297.
108. Tamuly, C., et al. (2014), *Reduction of aromatic nitro compounds catalyzed by biogenic CuO nanoparticles.* RSC Advances,. 4(95): p. 53229-53236.
109. Mohammadi-Aloucheh, R., et al. (2018), *Enhanced anti-bacterial activities of ZnO nanoparticles and ZnO/CuO nanocomposites synthesized using Vaccinium arctostaphylos L. fruit extract.* Artificial Cells, Nanomedicine, and Biotechnology,. 46(sup1): p. 1200-1209.
110. Karthik, P., T.N. Kumar, and B. Neppolian, *Redox couple mediated charge carrier separation in g-C_3N_4/CuO photocatalyst for enhanced photocatalytic H2 production.* International Journal of Hydrogen Energy, 2020. 45(13): p. 7541-7551.
111. Zhao, K., et al. (2015), *Importation and recombination are responsible for the latest emergence of highly pathogenic porcine reproductive and respiratory syndrome virus in China.* Journal of virology, 89(20): p. 10712-10716.
112. Ye, S., et al. (2019), *Facile assembled biochar-based nanocomposite with improved graphitization for efficient photocatalytic activity driven by visible light.* Applied Catalysis B: Environmental,. 250: p. 78-88.

113. Divya, N.,et al. 2017 *Photoluminescence quenching and photocatalytic enhancement of Pr-doped ZnO nanocrystals.* Bulletin of Materials Science,. 40(7): p. 1405-1413.
114. Panchal, P., et al. (2020), *Biogenic mediated Ag/ZnO nanocomposites for photocatalytic and antibacterial activities towards disinfection of water.* Journal of Colloid and Interface Science,. 563: p. 370-380.
115. V. Mohana, et al(2018), *Study of Ni: CeO2 nanoparticles for efficient photodegradation of methylene blue by sun light irradiation.* Indian Journal of Physics,. 92(12): p. 1601-1612.
116. Guo, H., et al. (2019), *Integrating the plasmonic effect and pn heterojunction into a novel Ag/Ag2O/PbBiO2Br photocatalyst: Broadened light absorption and accelerated charge separation co-mediated highly efficient visible/NIR light photocatalysis.* Chemical Engineering Journal,. 360: p. 349-363.
117. Joo, J., et al. (2013), *Magnetically recoverable hybrid TiO2 nanocrystal clusters with enhanced photocatalytic activity.* Materials Letters,. 93: p. 141-144.
118. Hankare, P., et al. (2011), *Enhanced photocatalytic degradation of methyl red and thymol blue using titania–alumina–zinc ferrite nanocomposite.* Applied Catalysis B: Environmental,. 107(3-4): p. 333-339.
119. Rai, P., et al. (2014), *Functionalization of ZnO nanorods by CuO nanospikes for gas sensor applications.* RSC Advances,. 4(45): p. 23604-23609.
120. Wilson, R.G. (1966), *Vacuum Thermionic Work Functions of Polycrystalline Be, Ti, Cr, Fe, Ni, Cu, Pt, and Type 304 Stainless Steel.* Journal of Applied Physics,. 37(6): p. 2261-2267.